

## Methods for Multi-Parametric Quantitative MRI

van Valenberg, W.

**DOI**

[10.4233/uuid:155ea22f-6686-4196-a270-743613ad1c33](https://doi.org/10.4233/uuid:155ea22f-6686-4196-a270-743613ad1c33)

**Publication date**

2020

**Document Version**

Final published version

**Citation (APA)**

van Valenberg, W. (2020). *Methods for Multi-Parametric Quantitative MRI*. [Dissertation (TU Delft), Delft University of Technology]. <https://doi.org/10.4233/uuid:155ea22f-6686-4196-a270-743613ad1c33>

**Important note**

To cite this publication, please use the final published version (if applicable). Please check the document version above.

**Copyright**

Other than for strictly personal use, it is not permitted to download, forward or distribute the text or part of it, without the consent of the author(s) and/or copyright holder(s), unless the work is under an open content license such as Creative Commons.

**Takedown policy**

Please contact us and provide details if you believe this document breaches copyrights. We will remove access to the work immediately and investigate your claim.

# Methods for Multi-Parametric Quantitative MRI



# Methods for Multi-Parametric Quantitative MRI

## DISSERTATION

for the purpose of obtaining the degree of doctor  
at Delft University of Technology,  
by the authority of the Rector Magnificus Prof. Dr. ir. T.H.J.J. van der Hagen;  
Chair of the Board for Doctorates,  
to be defended publicly on  
Friday 18 September 2020 at 10:00 o'clock

by

Willem VAN VALENBERG

Master of Science in Mathematics, Utrecht University  
born in Wageningen, The Netherlands

This dissertation has been approved by the promotors.

Composition of the doctoral committee:

Rector Magnificus,	chairperson
Prof.dr.ir. L.J. van Vliet	Delft University of Technology, <i>promotor</i>
Dr. F.M. Vos	Delft University of Technology, <i>promotor</i>
Dr. D.H.J. Poot	Erasmus Medical Center, <i>copromotor</i>

Independent members:

Prof.dr. W.J. Niessen	Delft University of Technology
Prof.dr. A.G. Webb	Leiden University Medical Center
Prof.dr. J. Sijbers	University of Antwerp
Prof.dr. J.A. Hernandez-Tamames	Erasmus Medical Center
Prof.dr. A.M. Vossepoel	Delft University of Technology, <i>reserve member</i>

Other members:

Dr.ir. S. Klein	Erasmus Medical Center
-----------------	------------------------



The work in this thesis was conducted at the Quantitative Imaging Group (QI), Faculty of Applied Sciences, Delft University of Technology, and at the Biomedical Imaging Group Rotterdam (BIGR), Faculty of Radiology, Erasmus Medical Center.

The work was funded by the Netherlands Organization for Health Research and Development ZonMW (project number 104 003 005).

Printed by: GVO drukkers & vormgevers B.V.

Copyright © 2020 by Willem van Valenberg

A digital copy can be downloaded from [repository.tudelft.nl](https://repository.tudelft.nl).

## Contents

<b>1</b>	Introduction .....	7
<b>2</b>	Dictionary Fitting.....	19
<b>3</b>	Time Efficiency.....	47
<b>4</b>	Protocol Optimization.....	67
<b>5</b>	Conclusions and Discussion.....	81
<b>R</b>	Reference List .....	87
<b>S</b>	Summary/Samenvatting.....	93
<b>A</b>	Acknowledgements .....	97
<b>P</b>	Publications .....	99
<b>CV</b>	Curriculum Vitae.....	101



# Introduction

Magnetic resonance imaging (MRI) has become a key medical imaging modality since its inception in the 1970s. An advantage of MRI over other modalities such as CT or PET is that the patient is not exposed to ionizing radiation. Additionally, the clinical success of MRI derives from its capacity to generate a large variety of contrasts between tissues. As such, MRI is currently an irreplaceable radiological tool for medical diagnosis, monitoring of diseases, and the planning of surgery. This chapter deals with some of the underlying physics of MRI and specifically the topics that are relevant for the rest of the thesis.

### ***Fundamentals of MRI***

MRI relies on the fact that atoms having unpaired protons or unpaired neutrons are magnetized when submerged in a strong magnetic field. In clinical practice, hydrogen nuclei are predominantly used, since hydrogen is abundantly present in the human body. Effectively, the magnetic moments of these hydrogen nuclei (commonly referred to as ‘spins’) tend to align with the main magnetic field of the MRI scanner. On a macroscopic scale, i.e. on the order of a  $\text{mm}^3$ , a net magnetization pointing along the main magnetic field direction is thus generated.

The spins in an external magnetic field also experience a torque that causes them to precess around the magnetic field: the so-called Larmor precession. The Larmor precession frequency  $\omega_L$  is determined by the strength of the external magnetic field  $B_0$  and the particle-specific gyromagnetic ratio  $\gamma$ :

$$\omega_L = \gamma B_0 \quad (1.1)$$

which, for hydrogen, is 42.58 MHz/Tesla and thus  $\omega_L$  lies in the radiofrequency (RF) range at the clinically used field strengths of 1.5 and 3 Tesla (T).

Excitation is achieved by subjecting the net magnetic moment to a secondary, oscillating electromagnetic field  $B_1$  of the same frequency as the Larmor frequency and perpendicular to  $B_0$ . As a result the magnetization vector will start to also rotate around the  $B_1$  field, see Figure 1.1. Effectively, the net magnetization vector is then tipped over by a certain angle: the flip angle ( $FA$ ), which is determined by the time-integral of the amplitude of the RF-pulse.

The transverse component of the precessing spins generates an oscillating electromagnetic field that induces an alternating current in a receive coil placed at a small dis-

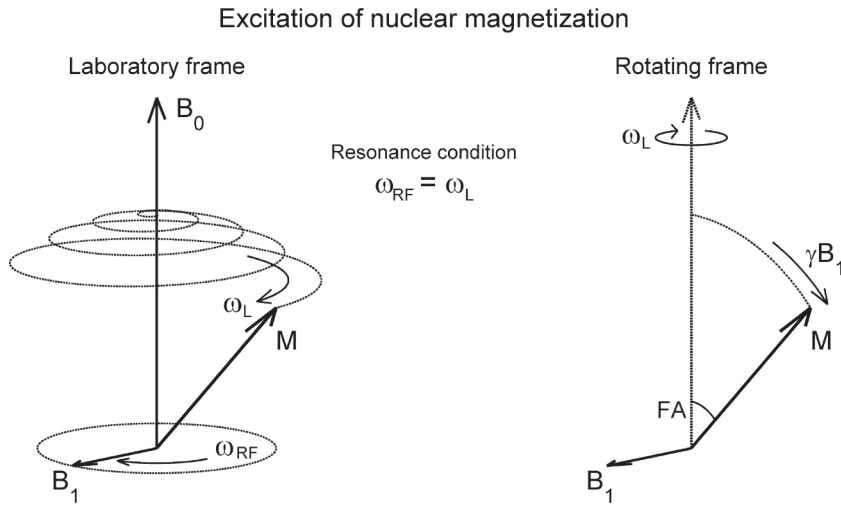


**Figure 1.1.** Combined effect of the static field magnetic field  $B_0$  and the oscillating magnetic field  $B_1$  on the net magnetization: the  $B_0$  field induces a precessional motion around its axis while the  $B_1$  field makes that the net magnetization is tilted towards the transverse plane. Image taken from Storey (2006).

tance. Thus, due to the application of RF-pulse, the net transverse magnetization becomes nonzero, and a signal can be detected. After spins have been excited by an RF-pulse, however, they will gradually relax back to their equilibrium state. On a macroscopic scale, this causes the longitudinal component of the net magnetization to recover to equilibrium in an exponential fashion. The relaxation time associated with this recovery is called the  $T_1$ -time and is illustrated in Figure 1.2.

Simultaneously, the spins also exchange energy among each other by a process called

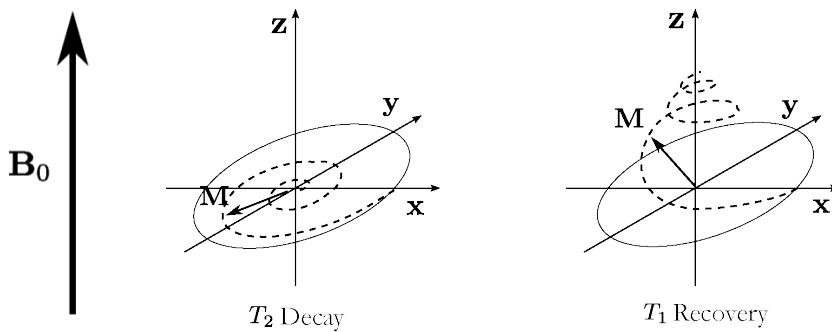


**Figure 1.2.** Illustration how the combined effect of the  $B_0$  field,  $T_1$  and  $T_2$  relaxation affect the signal after excitation. Image taken from Hazra (2016).

spin-spin interaction. This causes the relative phase of individual nearby spins to disperse, which results in the transverse component of the net magnetization decaying to zero. This is again an exponential process, characterized by the  $T_2$ -relaxation time and illustrated in Figure 1.2. Additionally, spins may experience static fluctuations in magnetic field strength, due to global variation in the  $B_0$  field, and/or susceptibility effects. Similar to the spin-spin interaction, this causes the individual spins to dephase, again resulting in an exponential decay of the transverse magnetization, characterized by the relaxation time  $T_2'$ . Since the  $T_2$  and  $T_2'$  effects both affect the transverse magnetization, they are often combined into one value known as  $T_2^* = 1/(1/T_2 + 1/T_2')$ .

The excited spins by default generate a signal at the same frequency irrespective of location, and are therefore indistinguishable. Hence, a mechanism is needed to spatially resolve the signal, i.e. to generate an image through spatial encoding. To facilitate spatial localization of the signal a magnetic field gradient is applied while applying a band-limited RF-pulse. The magnetic field gradient causes the Larmor frequency to vary linearly in space, so that only in a (thin) slice of the object the spins precess with a Larmor frequency inside the bandwidth of the RF-pulse and only those will be tilted into the transverse plane. Similarly, magnetic field gradients are applied during signal measurement. This also causes spins at different locations to precess at different Larmor frequencies. With clever control of the three magnetic field gradients ( $G_{read}$ ,  $G_{phase}$ ,  $G_{slice}$ ) in the MR system, it is possible to spatially encode each of the principal directions. A Fourier transform is applied to the acquired signal to reveal the encoded frequency components and implicitly resolves the spatial origin of its constituting components.

The bulk behavior of the spins is, in addition to  $T_1, T_2, T_2'$  relaxation, also influenced by physical processes such as water diffusion, blood flow, and oxygen consumption. By varying acquisition settings, these different physical processes can be emphasized in the acquired MR signal from which an image is created by means of a reconstruction method. The manner in which an MRI acquisition manipulates the signal in order to arrive at a certain image contrast is captured in an MR pulse sequence. Figure 1.3 exemplifies the versatility of acquisitions sequences for imaging the brain [1].

In practice, the contrast in MR images results from a mixture of physical properties of both the tissues and the scanning system. Importantly, the variation in intensity within an image, or between different images, is not directly linked to a single physical

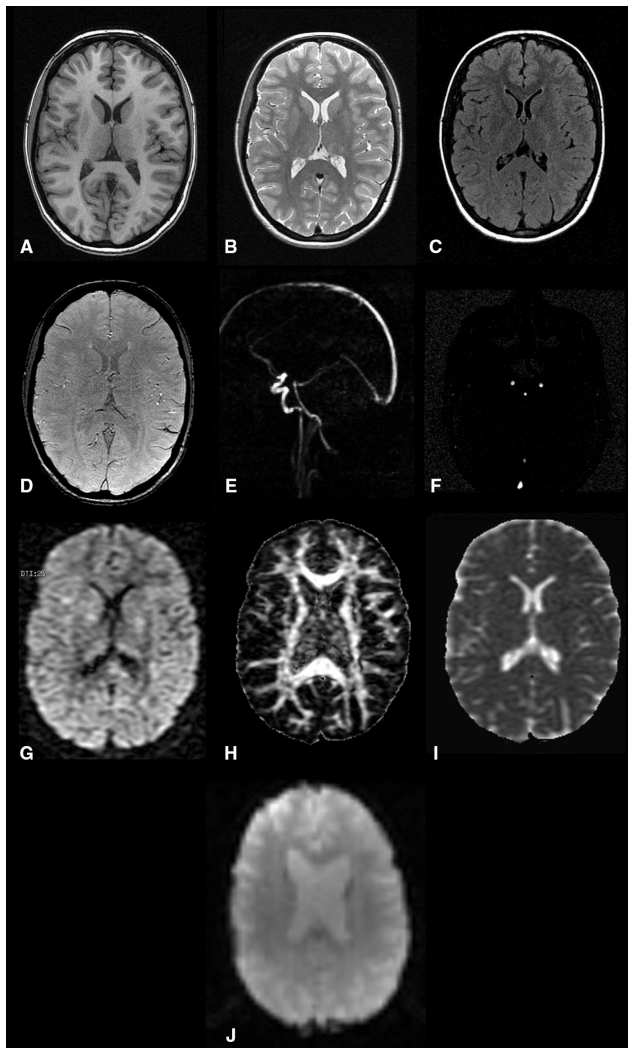


**Figure 1.3.** Example images of the brain using settings to emphasize (contrast due to)  $T_1$  relaxometry (A), proton density (B),  $T_2$  relaxometry (C),  $T_2^*$  relaxometry (D), flow (E-F), diffusion (G-I), and oxygen level (J). These images were acquired in the Rotterdam Scan Study (Ikram et al, 2015).

process. For instance, the contrasts in Figure 1.3 are influenced by the magnetic field that has both spatial and temporal variation due to fluctuation in the system and the interplay with the scanned object (in particular its susceptibility). Consequently, repeating a scan on the same or a different system will yield variation in image intensity due to essentially irrelevant factors. This is not problematic for many medical applications that are often based on a structural, visual interpretation of the anatomy. How-

ever, it is widely recognized that increasing the reproducibility of the measurements might improve detection of subtle changes in the body and thus improve clinical assessments [2], [3].

### **Quantitative MRI**

Quantitative MRI (qMRI) methods aim to obtain more reproducible data by measuring the separate physical processes that determine the MR signal. Changes in the parameters that represent these processes have been linked to various pathologies [2]. Furthermore, the physical basis of the measurements can help in the interpretation of changes. There are numerous methods for quantifying these physical parameters. This thesis concentrates on *relaxometry* methods that attempt to estimate the parameters that describe magnetic relaxation ( $T_1, T_2, T_2^*$ ), whose accurate estimation often requires the estimation of the static ( $B_0$ ) and RF transmit ( $B_1^+$ ) magnetic fields (see Figure 1.4).

Application of relaxometry methods is not commonly used for standard patient care in the clinic since traditionally these methods require long scan times. Furthermore, inaccuracy and variation in reported relaxometry values for common tissues is a known issue, which can be caused by ignoring physical effects in order to simplify the parame-

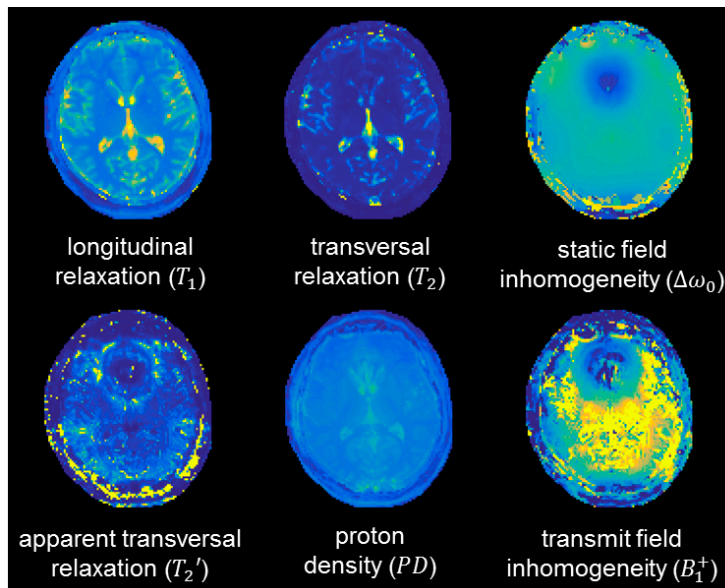


**Figure 1.4.** Parameter maps related to relaxometry, proton density, and magnetic fields in the brain.

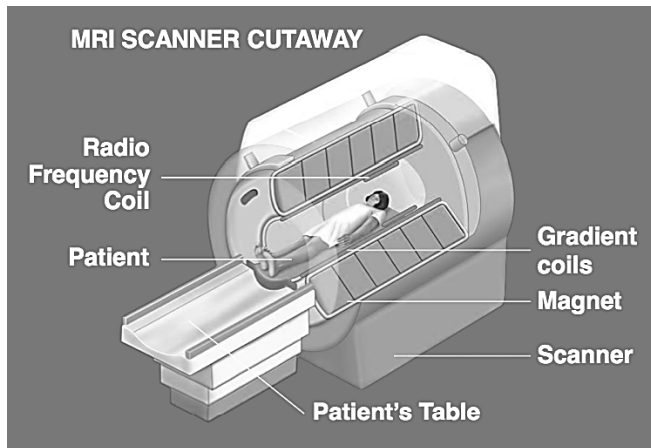


**Figure 1.5.** Overview MR scanner with special attention to the gradient, RF, and main magnetic field.

ter estimation.

In recent years, the research interest in qMRI methods has increased, in particular due to the introduction of efficient methods that are able to estimate multiple parameters in a short scan time [4]–[6]. Most notably, magnetic resonance fingerprinting (MRF) is a new paradigm for efficient parameter estimation that has received large interest in the MR research community [6].

In order to detail some of the issues of qMRI and the solutions offered in this thesis, the following part of this introduction will briefly address some of the relevant background information. A more extensive discussion of fundamental MR physics is provided in Haacke et al. [7].

### ***Modelling the MR system: the Bloch equations***

An MRI system as shown in Figure 1.5 obtains a signal from the hydrogen in the body through the generation and manipulation of magnetic fields. These magnetic fields consist of three components:

1. a strong homogeneous static magnetic field directed parallel to the bore in which the patient is lying.
2. gradient fields that can linearly increase or decrease the static field in any direction.
3. a radiofrequency (RF) field that is orthogonally directed to the static field.

In the following the bulk magnetic moment generated by the spins of a small volume element (voxel) at any time is represented by the vector  $M(t)$ . The behavior of this magnetization vector  $M(t)$  in the presence of the external magnetic field  $B(t)$  is described by the Bloch equation:

$$\frac{dM(t)}{dt} = \gamma M(t) \times B(t) + \frac{1}{T_1} (M_0 - M_z(t)) - \frac{1}{T_2} M_{xy}(t), \quad (1.2)$$

where  $\gamma \in \mathbb{R}$  is the gyromagnetic ratio and  $M_0$  represents the magnetization in its equilibrium state that scales with the local proton density ( $PD$ ). The vectors  $M_z$  and  $M_{xy}$  are respectively the projections of  $M$  parallel and orthogonal to the main magnetic field.

In the Bloch equation, the first term on the right describes the precessional behavior of the  $M(t)$  around the applied magnetic field  $B(t)$ , as illustrated in Figure 1.1. Here,  $B(t)$  is the sum of the constant  $B_0$  field, and the time-varying gradient ( $G_{read}, G_{phase}, G_{slice}$ ) and RF-transmit ( $B_1^+$ ) fields. The second and third term on the right describe respectively the  $T_1$  relaxation towards the main magnetic field ( $z$ -direction) and the  $T_2$  decay, as shown in Figure 1.2. While  $B(t)$  varies continuously over time, for simulation purposes we will assume that it is constant on small time intervals  $\Delta t$ . By alternating the relaxation and rotation steps, a simulation of the Bloch equation gets an accuracy of  $\mathcal{O}(\Delta t^2)$ , see [8].

Unfortunately, there are spatial variations in the applied magnetic fields particularly due to imperfections of the main magnetic field and the magnetic susceptibility of the scanned object. Static field inhomogeneities  $\Delta B_0$  affect the frequency of the rotating spins and thus their resonance. In addition, the inhomogeneity in  $B_1^+$  locally influences the ‘effectiveness’ of the RF pulses. Accounting for these magnetic field inhomogeneities is required for an accurate simulation of the MR signal.

### ***Quantitative methods: pulse sequences***

The Bloch equations reflect the dependence of the signal on the underlying physical parameters. Conversely, a physical parameter can be estimated from the evolution of the MR signal if a known sequence of timed excitation pulses is applied. Such a sequence is designed to separate the parameter(s) of interest from the confounding pa-

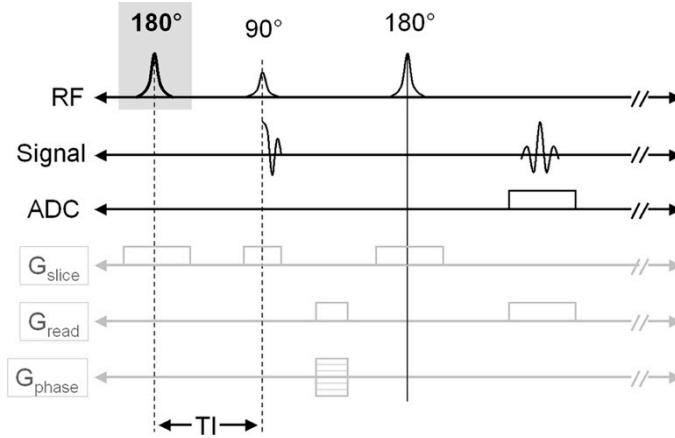
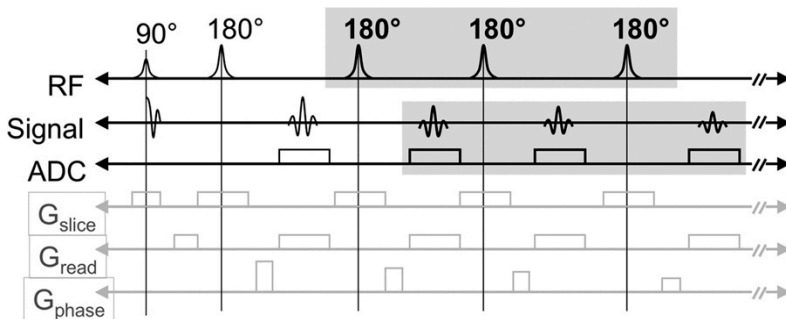


**Figure 1.6.** Diagram of inversion-recovery spin-echo (IRSE) sequence. Image taken from Pooley (2005). TI is the so-called inversion time, i.e. the time between the preceding  $180^\circ$  preparation pulse and the  $90^\circ$  pulse that is applied for imaging purposes.

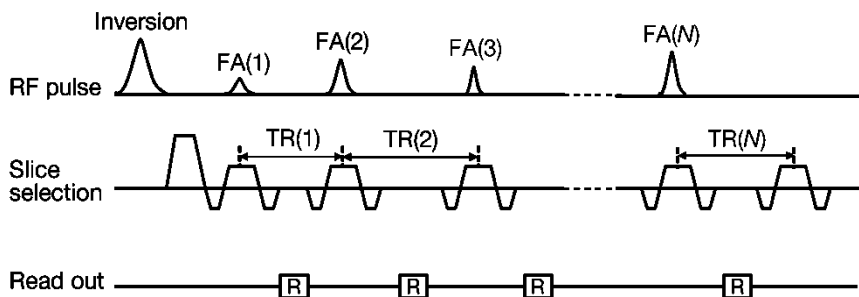
parameters. We illustrate this with three examples of qMRI sequences that are often applied for physical parameter estimation.

Figure 1.6 shows the pulse sequence of an inversion recovery method, which is used for  $T_1$  estimation. Initially, an inversion pulse ( $180^\circ$ ) is applied to reverse the magnetization. Subsequently excitation ( $90^\circ$ ) and refocusing ( $180^\circ$ ) pulses are applied to sample the signal after some inversion time TI, during longitudinal recovery. Notably, the parameters  $T_2$ , PD and variation in the  $B_1^+$  field induce a constant scaling of the measured signal, while the effect of  $\Delta B_0$  and  $T_2'$  is cancelled due to the refocusing pulse. Eventually, the  $T_1$  parameter can be estimated by fitting a simple exponential increasing function to the signal sampled at different inversion times.

Figure 1.7 shows the pulse sequence of a multiple-spin echo sequence, which is ap-



**Figure 1.7.** Diagram of multiple spin-echo (MSE) sequence. Image taken from Pooley (2005).



**Figure 1.8.** Diagram of magnetic resonance fingerprinting (MRF) sequence that applies radiofrequency pulses with varying flip angles (FA) and repetition times (TR). Image taken from Ma (2013).

plied to estimate the  $T_2$  parameter. After an excitation pulse, a sequence of refocusing pulses at fixed intervals are used to compensate for  $T_2'$  effects. Subsequently, an exponential decay function is fitted in order to derive the  $T_2$  relaxation constant. While doing so  $T_1$  influences are ignored and the  $B_1^+$  field is assumed to be constant.

Figure 1.8 shows the pulse sequence of a magnetic resonance fingerprinting (MRF) method, which was recently introduced to estimate multiple parameters in a single scan [6]. This method applies a sequence of RF pulses with pseudorandom flip angles and repetition times. Consequently, the measured signal does not follow a simple function of a single parameter, but requires solving the Bloch equation one time step at a time. The computational complexity of the Bloch equations makes parameter estimation through an iterative fitting procedure time-consuming. Therefore, the MRF method avoids repeated Bloch simulations by matching the measured signal to a pre-computed signal look-up table, or dictionary.

### **Research problems**

Although relaxometry methods improve the reproducibility and interpretability of data compared to conventional MRI, some issues have prevented the widespread application of quantitative methods to the clinic. The golden standard relaxometry methods have prohibitively long scan times, while faster methods often have low precision and/or accuracy. Practical application requires combining short scan times for each parameter of interest, with high accuracy and precision.

Magnetic Resonance Fingerprinting (MRF) is a promising method for estimating multiple parameters in a short scan time. However, parameter estimation through the

matching of measurements with a signal dictionary quickly becomes infeasible when increasing the number of estimated parameters due to high computational and memory costs. This limits the development of MRF methods with high precision for all relevant parameters.

Alternatively, multiple parameters can be estimated in a single scan through a protocol combining conventional qMRI methods, such as the inversion-recovery spin-echo (IRSE) and multiple spin-echo (MSE) methods. However, this requires an increase in the accuracy and precision these methods obtain in a short scan time. The accuracy can improve by estimating all relevant parameters simultaneously and sharing information between the separate qMRI methods. Higher precision might be obtained by carefully selecting which methods to include in the protocol and with which settings. But this requires a practical method for comparing the precisions of qMRI methods over a wide range of settings, which currently is unavailable.

### ***Research aim***

In this work we aim to facilitate quantitative, reproducible estimation of multiple physical MRI parameters. In order to do so, our research has focused on developing novel methods for:

- 1) reducing the computational and memory requirements of the estimation of parameters with increased dimensionality.
- 2) selecting the most appropriate qMRI method as well as its settings, i.e. the MRI method with the highest precision in the available scan time.
- 3) designing scan protocols for the simultaneous estimation of multiple parameters from the combination of qMRI methods with highest precision.

### ***Outline***

The current chapter described the aim of this thesis and the relevant background information.

**Chapter 2** presents an efficient method for the simultaneous estimation of multiple parameters from quantitative methods such as MRF. This is done by approximating the signal model over the parameter range through B-spline interpolation. Consequently, the parameter estimation obtains equal accuracy as the conventional dictionary

matching, while reducing the computational and memory requirements with an order of magnitude per estimated parameter.

**Chapter 3** introduces a framework to assess the time efficiency as a quality measure for quantitative methods. Time efficiency equals the precision obtained in a unit of scan time. We validate the predicted time efficiency on the scanner over a wide range of different qMRI methods.

**Chapter 4** implements a framework for the design of a scan protocol for the estimation of the relaxometry parameters ( $T_1, T_2, T_2'$ ) with optimal time efficiency. We show that the optimized protocols can estimate multiple parameters simultaneously and with higher precision than most traditional quantitative methods with the same scan time.

**Chapter 5** discusses the strengths and weaknesses of the methods introduced in this thesis and gives an outlook for future developments.

# Dictionary Fitting

Contents of this chapter was published in IEEE Transactions on Medical Imaging as

## An Efficient Method for Multi-Parameter Mapping in Quantitative MRI using B-Spline Interpolation

Willem van Valenberg, Stefan Klein, Frans M. Vos, Kirsten Koolstra, Lucas J. van Vliet, Dirk H.J. Poot

### Abstract

Quantitative MRI methods that estimate multiple physical parameters simultaneously often require the fitting of a computational complex signal model defined through the Bloch equations. Repeated Bloch simulations can be avoided by matching the measured signal with a precomputed signal dictionary on a discrete parameter grid (i.e. lookup table) as used in MR Fingerprinting. However, accurate estimation requires discretizing each parameter with a high resolution and consequently high computational and memory costs for dictionary generation, storage, and matching.

Here, we reduce the required parameter resolution by approximating the signal between grid points through B-spline interpolation. The interpolant and its gradient are evaluated efficiently which enables a least-squares fitting method for parameter mapping. The resolution of each parameter was minimized while obtaining a user-specified interpolation accuracy. The method was evaluated by phantom and in-vivo experiments using fully-sampled and undersampled unbalanced (FISP) MR fingerprinting acquisitions. Bloch simulations incorporated relaxation effects ( $T_1, T_2$ ), proton density ( $PD$ ), receiver phase ( $\varphi_0$ ), transmit field inhomogeneity ( $B_1^+$ ), and slice profile. Parameter maps were compared with those obtained from dictionary matching, where the parameter resolution was chosen to obtain similar signal (interpolation) accuracy. For both the phantom and the in-vivo acquisition, the proposed method approximated the parameter maps obtained through dictionary matching while reducing the parameter resolution in each dimension ( $T_1, T_2, B_1^+$ ) by – on average – an order of magnitude. In effect, the applied dictionary was reduced from 1.47 GB to 464 KB. Furthermore, the proposed method was equally robust against undersampling artifacts as dictionary matching. Dictionary fitting with B-spline interpolation reduces the computational and memory costs of dictionary-based methods and is therefore a promising method for multi-parametric mapping.

## Introduction

Quantitative MRI (qMRI) methods measure the magnetic properties of tissues, described by parameters such as relaxation times ( $T_1, T_2, T_2^*$ ) and proton density ( $PD$ ). Many of these methods require knowledge of inhomogeneities in the static ( $\Delta B_0$ ) and/or transmit ( $B_1^+$ ) magnetic field in order to obtain accurate parameter maps. Changes in the magnetic properties of tissues have been linked to various pathologies [2].

Magnetic resonance fingerprinting (MRF) is a recently introduced paradigm to acquire multiple parameters within a short scan time [6]. MRF methods use a pulse sequence with varying flip angles and repetition times to acquire images with many different contrasts. In each voxel, the signal's time course is assumed to be specific to the parameter combination representing the underlying tissue. Usually, each contrast is undersampled, but by varying the k-space trajectory among the contrasts, undersampling artifacts are assumed separable from the true signal of a voxel. Parameter estimation is done by matching the acquired signal course in a voxel to a dictionary that contains the simulated signals, or atoms, for a grid of parameter combinations (e.g.  $T_1, T_2, T_2^*, \Delta B_0, B_1^+$ ). This matching avoids the fitting of an explicit signal model, which in MRF would require repeatedly solving Bloch equations, which is computationally expensive. Before MRF, dictionary matching was also applied in other qMRI methods in order to improve  $T_1$  estimation [9], [10],  $T_2$  estimation [11], and water/fat separation [12], [13].

The original MRF paper obtained  $T_1, T_2, \Delta B_0$ , and  $PD$  parameter maps with a pseudorandom 2D inversion-recovery balanced steady state free-precession (IR-bSSFP) sequence with variable-density-spiral readout [6]. Subsequently, a modification to the original scheme was proposed by applying the fast-imaging with steady-state precession (FISP) sequence, which includes unbalanced gradients [14]. This reduced the influence of static field inhomogeneities at the cost of a lower signal-to-noise ratio (SNR). In recent years, these MRF methods have been extended to measure other properties of interest such as diffusion [15], perfusion [16], and chemical exchange [17]. Furthermore, including transmit field inhomogeneity ( $B_1^+$ ) and slice profile in the fitting has been shown to increase the accuracy of the resulting relaxometry maps [18], [19].

However, dictionary matching becomes problematic when the number of estimated parameters is increased. The number of atoms increases exponentially with the number of parameters, and consequently also the computational and memory costs of generating, storing, and matching to the dictionary. This is especially prohibitive if the required precision for each parameter is high since this requires many steps along each dimension of the dictionary.

Several clever strategies were introduced to reduce the computational and memory demands of large dictionaries. Smarter search strategies can significantly reduce the matching time [20], but the size of the dictionary is limited by the available memory. The atoms can be compressed with a singular value decomposition (SVD) to lower the computational and memory costs for matching and storing the dictionary [21]. However, using too few singular vectors degrades the results. More recent work proposed interpolating the signal with a polynomial hyperplane fitted on a sparsely sampled dictionary [22]. However, this method was applied to a two-parameter case only ( $T_1$  and  $T_2$ ) and the accuracy of the parameter maps remained limited to an a priori defined refinement factor.

We propose parameter estimation by fitting the acquired MR signal with a continuous signal model defined through B-spline interpolation of a sparse dictionary. The interpolation targets to maintain the estimation accuracy while reducing the resolution of each parameter and consequently the computational and memory costs of the dictionary. This would enable the estimation of an increased number of parameters simultaneously. B-spline interpolation is commonly used in image interpolation because it is a flexible and efficient technique that has minimal support for a desired interpolation error [23], [24]. In particular, the derivative of the interpolant can be calculated efficiently [24] which allows a gradient-based optimization technique for fitting a measured signal to the dictionary. Additionally, we introduce a method to estimate the parameter resolution in the dictionary that is required to achieve a user-specified interpolation accuracy. The proposed method is evaluated on simulated data and measurements taken from phantom and in-vivo experiments. The efficiency of our dictionary fitting framework is compared to matching with a dictionary of equal accuracy. We hypothesize that the proposed method accurately estimates a comprehensive set of parameters based on a significantly smaller dictionary.

## Methods

### *Parameter Estimation*

A general qMRI method measures the complex-valued signal  $\mathbf{m}$  of a voxel at  $M$  time points. The signal is assumed to be a function of  $P$  parameters  $\boldsymbol{\theta} = [\theta_1, \dots, \theta_P] \in \Theta \subseteq \mathbb{R}^P$ , contaminated by Gaussian noise:

$$\mathbf{m} = \rho \mathbf{s}(\boldsymbol{\theta}) + \boldsymbol{\sigma} \quad (2.1)$$

The signal model  $\mathbf{s}(\boldsymbol{\theta}) \in \mathbb{C}^M$  is the pulse sequence specific solution of the Bloch equations, and the scaling factor  $\rho \in \mathbb{C}$  is dependent on the proton density and the receiver sensitivity. Note that we assume a single-compartment model in each voxel, so that  $\rho$  is a single complex number. The Gaussian noise  $\boldsymbol{\sigma} \in \mathbb{C}^M$  is considered identical and uncorrelated between measurements and receiver channels.

Parameter estimation is often done by least-squares fitting:

$$[\hat{\boldsymbol{\theta}}, \hat{\rho}] = \arg \min_{\boldsymbol{\theta} \in \Theta, \rho \in \mathbb{C}} \|\mathbf{m} - \rho \mathbf{s}(\boldsymbol{\theta})\|_2^2 \quad (2.2)$$

However, the signal model  $\mathbf{s}(\boldsymbol{\theta})$  is computationally complex for MRF, since the signal at a given time point depends on the signal's history during previous steps. As such, it requires solving the Bloch equations step-by-step. This makes conventional optimization techniques for solving Eq. 2.2 expensive.

### *Dictionary Matching*

MRF avoids repeated evaluation of  $\mathbf{s}(\boldsymbol{\theta})$  by matching the acquired signal to a pre-computed dictionary, i.e. signals on a discrete grid of parameter values [6]. The dictionary atom with index  $\mathbf{k} \in \mathbb{N}^P$  corresponds to parameter values  $\boldsymbol{\theta} = \mathbf{f}(\mathbf{k})$ , where the mapping  $\mathbf{f}(\mathbf{v})$  is defined for continuous grid position  $\mathbf{v} \in \mathbb{R}^P$  in order to facilitate interpolation (see below).

The dictionary matching step in MRF finds for a measured signal  $\mathbf{m}$  the grid point  $\hat{\mathbf{k}}$  and consequently the associated parameter combination  $\hat{\boldsymbol{\theta}} = \mathbf{f}(\hat{\mathbf{k}})$  by

$$\hat{\mathbf{k}} = \arg \max_{\mathbf{k}} |\mathbf{m}^H \mathbf{s}(\mathbf{f}(\mathbf{k}))| / \|\mathbf{s}(\mathbf{f}(\mathbf{k}))\|_2. \quad (2.3)$$

The superscript  $H$  indicates the Hermitian conjugate. The complex scaling factor  $\hat{\rho}$  is subsequently determined through the least-square solution:

$$\hat{\rho} = \left( \mathbf{s}(\hat{\boldsymbol{\theta}})^H \mathbf{m} \right) / \left( \mathbf{s}(\hat{\boldsymbol{\theta}})^H \mathbf{s}(\hat{\boldsymbol{\theta}}) \right) \in \mathbb{C} \quad (2.4)$$

The solution  $[\mathbf{f}(\hat{\mathbf{k}}), \hat{\rho}]$  of Eqs. 2.3 and 2.4 is also the solution of Eq. 2.2 when cast as a discrete optimization problem over the parameter values  $\boldsymbol{\theta} = \mathbf{f}(\mathbf{k})$  (see Supplementary Materials A).

The number of dictionary atoms increases linearly with the number of discretized values ( $K_p$ ) of each parameter and exponentially with the number of parameters ( $P$ ). Therefore, high-precision multi-parameter maps are computationally infeasible since the computational and memory cost for dictionary generation, storage, and matching scale linearly with the number of dictionary atoms. Singular value decomposition (SVD) can alleviate these effects by projecting both the measurement data  $\mathbf{m}$  and the dictionary atoms  $\mathbf{s}(\mathbf{f}(\mathbf{k}))$  to a lower dimensional space:

$$\begin{aligned} \mathbf{m}_L &= \mathbf{V}_L^T \mathbf{m} \in \mathbb{C}^L \\ \mathbf{s}_L(\mathbf{f}(\mathbf{k})) &= \mathbf{V}_L^T \mathbf{s}(\mathbf{f}(\mathbf{k})) \in \mathbb{C}^L \end{aligned} \quad (2.5)$$

where  $\mathbf{V}_L^T$  contains the singular vectors corresponding to the  $L$  largest singular values. As a result, the memory costs of storing the dictionary and the cost of the dictionary-matching step in Eq. 2.3 reduces by a factor  $L/M$  [14]. However, the results degrade when using too few singular vectors and multi-parameter mapping is still computationally demanding since the SVD only reduces the number of time points and not the number of atoms.

### **Dictionary Fitting**

To enhance the precision of the parameter maps while limiting the number of grid points, we propose a dictionary fitting<sup>1</sup> framework in which the signal is modelled on the whole, continuous parameter domain through interpolation of a sparsely sampled dictionary. We define the B-spline interpolated signal of order  $n$  at grid position  $\mathbf{v} \in \mathbb{R}^P$  (without SVD) as [23]:

---

<sup>1</sup>We use the term dictionary matching for the discrete optimization in Eq. 2.3 and dictionary fitting for the continuous optimization in Eq. 2.8.

$$\tilde{\mathbf{s}}(\mathbf{v}) = \sum_{\mathbf{k} \in \mathbb{N}^P} \mathbf{c}(\mathbf{k}) \boldsymbol{\beta}^n(\mathbf{v} - \mathbf{k}) \quad (2.6)$$

Here,  $\mathbf{c}(\mathbf{k}) \in \mathbb{C}^M$  indicates the B-spline coefficient for each dictionary atom and  $\boldsymbol{\beta}^n(\mathbf{v})$  is the product of B-spline basis functions of order  $n$  along each dimension:

$$\boldsymbol{\beta}^n(\mathbf{v}) = \prod_{p=1}^P \beta^n(v_p) \quad (2.7)$$

For details on B-spline interpolation, including the exact definition of the B-spline basis functions  $\beta^n(v_p)$  we refer to a general background paper [23]. Essentially, the  $n$ th order B-spline basis function is a piecewise polynomial of degree  $n$  with width of support  $n + 1$ . The coefficients  $\mathbf{c}(\mathbf{k})$  can be obtained via a closed-form solution, such that  $\tilde{\mathbf{s}}(\mathbf{k}) = \mathbf{s}(\mathbf{f}(\mathbf{k}))$ . In effect, the interpolated function intersects the dictionary atoms exactly, while there is continuity up to the  $n$ th derivative.

With SVD compression, the B-spline interpolated signal  $\tilde{\mathbf{s}}_L(\mathbf{k}) \in \mathbb{C}^L$  and its coefficients  $\mathbf{c}_L(\mathbf{k}) \in \mathbb{C}^L$  are defined by replacing  $\mathbf{s}(\mathbf{f}(\mathbf{k})) \in \mathbb{C}^M$  with  $\mathbf{s}_L(\mathbf{f}(\mathbf{k})) \in \mathbb{C}^L$ . Through recursive implementation of the spline interpolation [24], the computational cost of evaluating both  $\tilde{\mathbf{s}}_L(\mathbf{v})$  and its gradient is only  $\mathcal{O}(Ln^P)$ . The incorporation of B-spline interpolation and SVD compression in Eq. 2.2 yields:

$$[\hat{\mathbf{v}}, \hat{\rho}] = \arg \min_{\mathbf{v}, \rho} \|\mathbf{m}_L - \rho \tilde{\mathbf{s}}_L(\mathbf{v})\|_2 \quad (2.8)$$

The optimization problem in Eq. 2.8 is solved using the `fmincon` routine from MATLAB (The Mathworks, Natick, MA) with the `trust-region-reflective` algorithm. Dictionary matching determines the initial value and the optimization stops when the error reduction is below  $10^{-5}$  in subsequent steps or after 100 iterations. Subsequently, we set  $\hat{\boldsymbol{\theta}} = \mathbf{f}(\hat{\mathbf{v}})$ , and the proton density (*PD*) and receiver phase ( $\varphi_0$ ) are determined by the modulus and phase of the complex scaling factor  $\hat{\rho}$ . The accuracy of the parameter estimates from Eq. 2.8 depends on the invertibility of the forward model  $\mathbf{s}(\boldsymbol{\theta})$  (i.e the applied acquisition), and on the approximation errors due to the SVD projection (Eq. 2.5) and the B-spline interpolation (Eq. 2.6) of which the latter is investigated in the following section.

### **Parameter Resolution**

The interpolation error over the range  $\Theta_p$  of parameter  $\theta_p$  decays as  $\mathcal{O}(K_p^{-n-1})$  for B-spline order  $n$  and number of discretized values  $K_p$  [23]. The interpolation error at a specific position  $\mathbf{v} \in \mathbb{R}^P$  is defined by

$$E_{int}(\mathbf{v}) := \|\tilde{\mathbf{s}}(\mathbf{v}) - \mathbf{s}(\mathbf{f}(\mathbf{v}))\|_2. \quad (2.9)$$

To reduce the computation and memory costs of the dictionary, we aim to find for each spline order the smallest number of atoms such that  $E_{int}(\mathbf{v})$  is below a user-specified threshold  $\alpha$  for all  $\mathbf{v}$  with  $\mathbf{f}(\mathbf{v}) \in \Theta$ . We set the parameter resolution of the dictionary based on the interpolation error on the boundary of  $\Theta$ , where we assume the error is maximal. So the parameter resolution of the dictionary is determined under the assumption that the interpolation error is maximal at the boundary of  $\Theta$ . Consequently, the number of atoms ( $K_p$ ) in parameter domain  $\Theta_p$  is estimated based on the interpolation error along  $2^{P-1}$  edges where the other parameters obtain their maximal/minimal value. On each edge, we define  $\tilde{\mathbf{s}}(\mathbf{v})$  through interpolation of increasing number of atoms  $K_p = 2^{j-1} + 1$  uniformly sampled on the grid, starting with  $j = 1$  (i.e. the minimum and maximum of parameter  $\theta_p$ ) until a user-specified maximum  $J$ . For each iteration  $j$  and spline order  $n$ , we determine the overall interpolation error as the maximum of  $E_{int}(\mathbf{v})$  evaluated at the midpoints between atoms on each edge. We select the  $K_p$  for which the overall interpolation error is below a chosen value  $\alpha$  for the given number and all further refinements. We include values  $K_p \neq 2^j + 1$  in this selection by estimating the overall interpolation error between the  $J$  iterations through linear interpolation.

### **Dictionary Design**

The dictionary-fitting framework is tested with a FISP MRF pulse sequence [14]. The generated dictionary contains the simulated signals as a function of  $P = 3$  parameters: longitudinal relaxation time  $T_1 \in [5, 6000]$  ms, transversal relaxation time  $T_2 \in [5, 2000]$  ms, and transmit field inhomogeneity  $B_1^+ \in [0.5, 1.5]$ . Thus  $\boldsymbol{\theta} = (T_1, T_2, B_1^+) \in \mathbb{R}^3$ . We define  $\boldsymbol{\theta} = \mathbf{f}(\mathbf{v}) = [f_1(v_1), f_2(v_2), f_3(v_3)]$ , where  $f_p$  maps  $[1, K_p]$  to  $\Omega_p$  logarithmically for  $T_1$  and  $T_2$ , and linearly for  $B_1^+$ . This choice was made since the signal amplitude has a known exponential dependence on  $T_1$  and  $T_2$ . For B-spline orders  $n \geq 2$ , we avoid interpolation issues near the boundary by extend-

ing the grid with one position outside of  $\Theta$  and set the derivative of the interpolant equal the numerical derivative as boundary condition.

The pulse sequence was modelled with an event-based approach with RF pulses, gradient pulses, and signal readout at specified time points. Adiabatic inversion pulse and gradient pulses were modelled as instantaneous rotations. The slice profile was modelled through 10,000 spins that were uniformly distributed over twice the slice width (FWHM). To reduce computational complexity, the true excitation pulse was replaced by a pulse consisting of 7 time steps with amplitude, phase, and duration of each step optimized to approximate the true response of a 90 degree pulse without relaxation. This approximation had a relative error below 1% (with  $L^2$  norm) and reduced the computational complexity by a factor of 14 compare to applying the full RF pulse. The simulated signal  $\mathbf{s}(\boldsymbol{\theta})$  has the maximal amplitude of 1 when all spins are coherent in the transverse plane.

## Experiments

The proposed approach was evaluated on simulated, phantom, and in-vivo data. In each experiment, we used 1000 flip angles and repetition times as specified in the original FISP MRF article [14]. Other settings were: inversion time  $T_I = 40$  ms, echo time  $T_E = 2.5$  ms, and delay  $T_D = 5000$  ms after each pulse train. Excitation pulses had a duration of 1 ms, a time-bandwidth product of 3, and a slice width of 5 mm.

The code of the dictionary fitting framework and the experiments performed is provided for reference purposes at [https://bitbucket.org/bigr\\_erasmusmc/dictionary\\_fitting](https://bitbucket.org/bigr_erasmusmc/dictionary_fitting). All processing was done in MATLAB using a single 2.1 GHz core (AMD Opteron 6172).

### *Dictionary Design and Generation*

The resolution of the parameters in the dictionary was estimated for each combination of pulse sequence and spline order (see “Parameter Resolution”). We set the interpolation error threshold to  $\alpha = 5 \cdot 10^{-4}$ , which is below the noise level observed in our practical experiments, and the maximum number of iterations  $J = 10$ , since higher number of atoms were computationally infeasible. The total dictionary size was calculated as the product of required number of atoms for each parameter to pass the target error.

Two dictionaries were generated in order to evaluate the proposed method. Dictionary fitting (Eq. 2.8) used a sparse dictionary based on the parameter resolution prescribed for second ( $n = 2$ ) order B-spline interpolation. As a reference, parameter estimation was done through dictionary matching (Eq. 2.3) using a dense dictionary with parameter resolution prescribed for zeroth ( $n = 0$ ) order B-spline interpolation (i.e. nearest neighbor).

### ***Dictionary Evaluation***

We evaluate if the interpolation error in the interior is below the prescribed threshold  $\alpha$  in the dense and sparse dictionary with respectively zeroth and second order B-spline interpolation. The interpolation error was determined by Eq. 2.9 at a 1000 positions  $\mathbf{v}$ , sampled uniformly between 1 and  $K_p$  for each dimension  $p$ , with condition that  $f_2(v_2) = T_2 \leq T_1 = f_1(v_1)$  to ensure physically realistic values. This validation of the interpolation accuracy was performed without SVD compression in order to separate different sources of error.

### ***Phantom and In-vivo Experiment***

Practically, we evaluated the dictionary-fitting framework on a 3T Ingenia scanner with a 32-channel head coil (Philips Healthcare, Best, The Netherlands) on a phantom and a healthy volunteer. Data sampling was done using a spiral trajectory that was rotated 7.5 degrees between samples and required 48 interleaves to fully sample a  $128 \times 128$  matrix.

Parameter maps were determined by dictionary fitting (Eq. 2.8) and matching (Eq. 2.3) with respectively the sparse and dense dictionaries with SVD compression. The number of singular values  $L$  was set to 30 which is in accordance with previous work [22]. The effect of the compression was evaluated on the parameter maps obtained from the fully-sampled in-vivo experiment.

For the phantom experiment we used the NIST system phantom that contains contrast spheres with calibrated  $T_1$  and  $T_2$  values [25]. We reconstructed images based on an undersampled (1 interleave) and fully sampled (48 interleaves) acquisition. The total scan time was 18 and 871 seconds for the undersampled and fully sampled acquisition, respectively. The accuracy of the methods was compared through the relative difference between the mean estimated  $T_1$  and  $T_2$  values in each contrast sphere for both the fully sampled and undersampled data. To quantify the efficiency of our

method, we recorded the computation time and memory usage for the dictionary calculation, storage and fitting.

The in-vivo experiment concerned acquiring a 2D slice of the brain of a healthy volunteer. The study was approved by the LUMC review board for Medical Ethics and the volunteer gave an informed consent. Initially, we compare the parameter maps obtained with dictionary matching and fitting from reconstructed images of the fully sampled (48 interleaves) acquisition. Subsequently, we retrospectively undersampled the k-spaces of the fully sampled acquisition by selecting 1, 2, 4, 6, 12, 24, and 48 interleaves. Image reconstruction based on the selected interleaves was performed by a non-uniform Fourier transform with density compensation. For each number of interleaves, we determined the  $T_1$  and  $T_2$  maps obtained through dictionary matching and fitting, and compared those with the maps from the fully sampled data.

## Results

### *Dictionary Design and Generation*

Figure 2.1 shows the predicted interpolation error as a function of the number of atoms in each parameter dimension ( $K_p$ ) for spline orders  $n = \{0,1,2,3\}$ . The interpolation error was quantified by the maximum value of  $E_{int}(\mathbf{v})$  over the midpoints between sampled positions. The legend reports the minimum number of atoms required for  $E_{int}(\mathbf{v}) < 5 \cdot 10^{-4}$  (which excludes the boundary padding for  $n \geq 2$ ). The method predicts for zeroth order B-spline interpolation that the target interpolation error is achieved using  $7.05 \cdot 10^6$  atoms (i.e.  $454 \cdot 97 \cdot 160$ ). With second order spline, the total number of atoms including the boundary dropped to 2080 (i.e.  $13 \cdot 8 \cdot 20$ ), a factor of  $3.38 \cdot 10^3$  reduction.

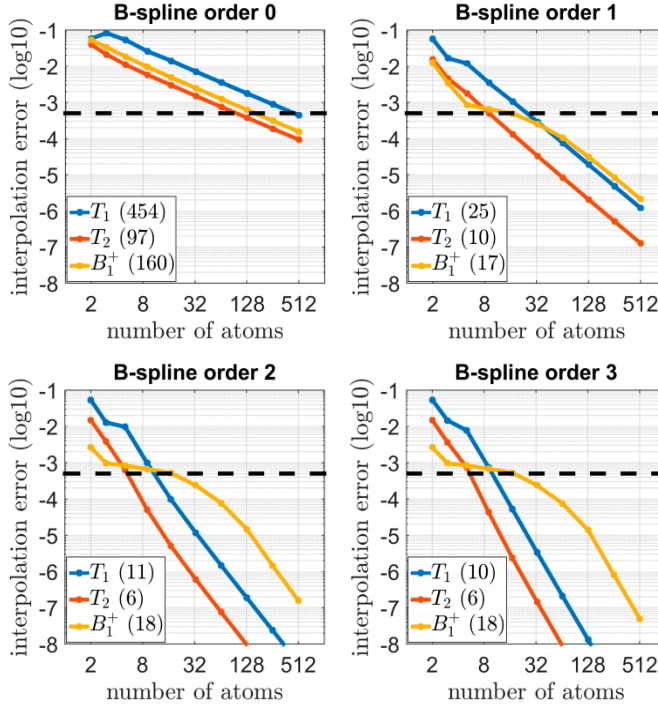


**Figure 2.1.** Interpolation error on the edge of parameter space as function of number of atoms in each dimension. Dashed line indicates target error and the legend shows for each parameter the minimum number of atoms required to obtain the target error. The number of atoms in each parameter dimension reduces approximately an order of magnitude between zeroth and higher order B-spline interpolation.

Dictionaries with both these parameter resolutions were generated. To do so the average computation time of a single atom based on the Bloch simulation was 6.20 seconds. SVD compression to 30 vectors reduced the memory cost of the dense dictionary from 48.0 GB to 1.47 GB, and of the sparse dictionary from 14.6 MB to 464 KB.

### Dictionary Evaluation

Figure 2.2 shows the interpolation error  $E_{int}(v)$  of a 1000 positions in the interior for the dense and sparse dictionaries with respectively zeroth and second order B-spline interpolation (without SVD). The interpolation errors are shown as function of  $T_1$ ,  $T_2$ , and  $B_1^+$ . Note that the constraint  $T_1 \geq T_2$  biased sampled positions to high  $T_1$  and low  $T_2$  values. The root-mean-square value of all interpolation errors was  $4.1 \cdot 10^{-4}$  and  $2.8 \cdot 10^{-4}$  for respectively the dense and sparse dictionary, with maxima of  $31 \cdot 10^{-4}$  and  $16 \cdot 10^{-4}$ . The interpolation error was above the target error for 15.5% of the sampled positions with dictionary matching, and for 7.0% of the

same sampled positions with dictionary fitting. It can be observed that in particular the interpolation error with second-order B-splines was highest for test signals with  $T_1$  and  $T_2$  values near the extremes of the parameter range (left and right sides of the graphs).

A single evaluation of the spline interpolation function and its gradient took 1.4 ms without SVD compression.

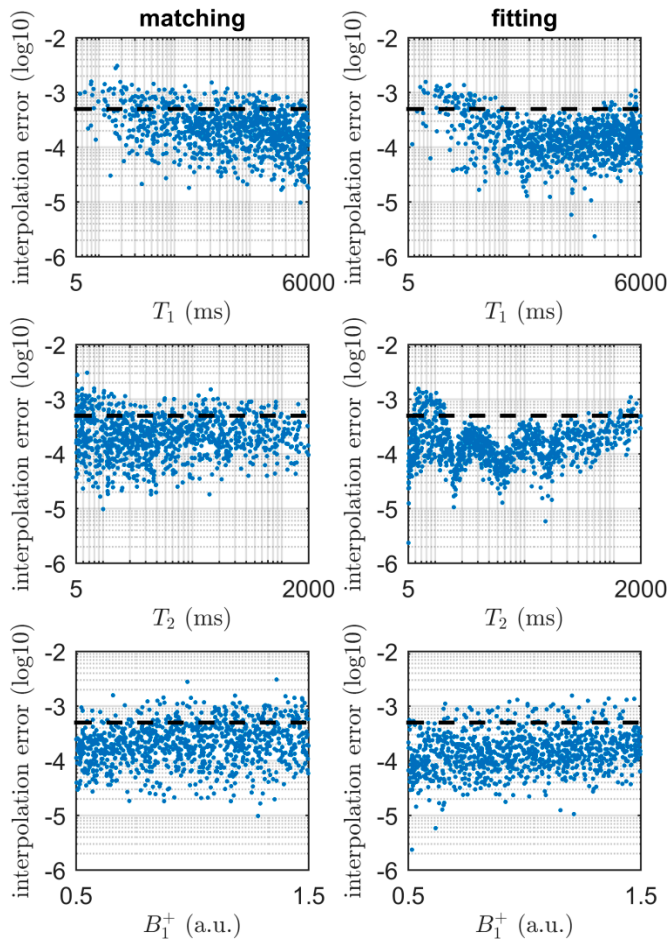
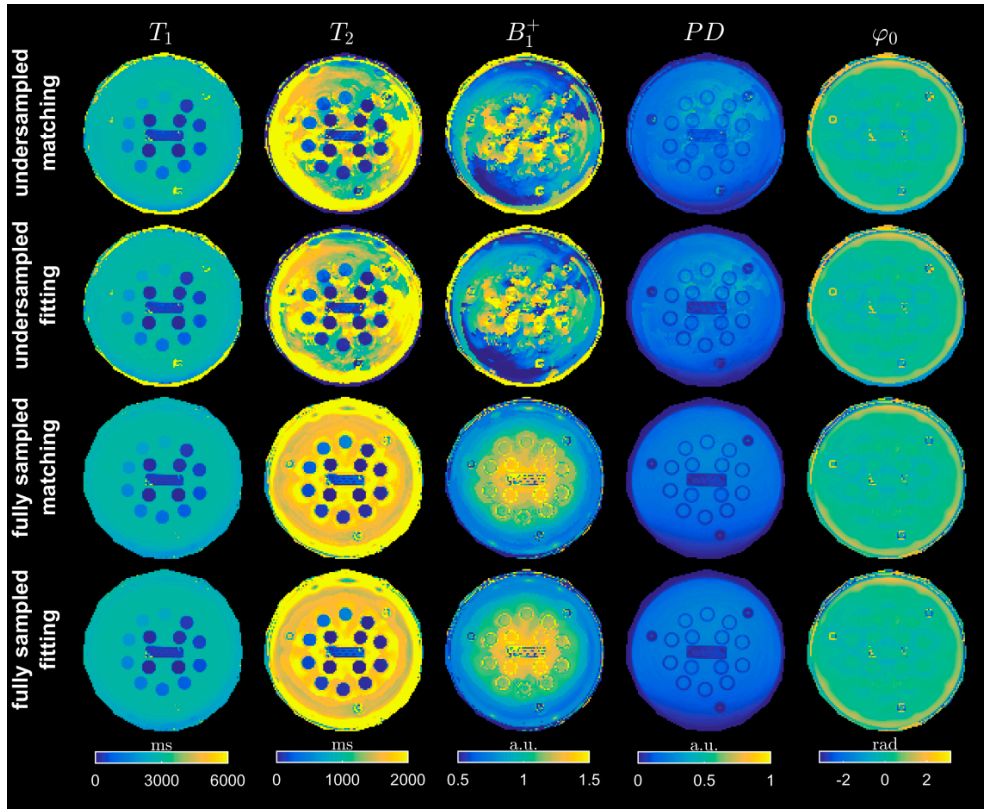


**Figure 2.2.** Interpolation error at 1000 uniformly sampled positions in the grid for the dictionary used with matching (left) and fitting (right). The dashed line indicates the target error applied for dictionary design. The parameter resolution of both dictionaries is sufficient to obtain the target error for most grid positions in the interior.

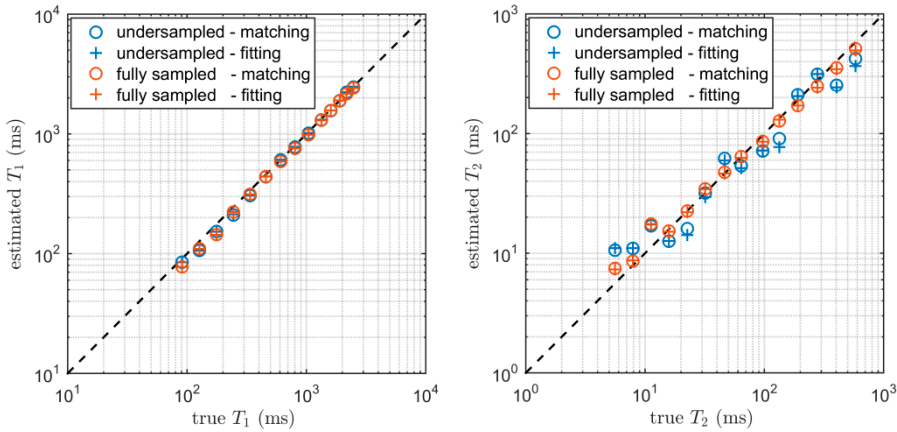
### Phantom Experiment

Figure 2.3 shows that both for the prospective undersampled and fully sampled acquisitions the parameter maps obtained with dictionary matching were closely approximated by the proposed dictionary fitting method. The  $T_2$ ,  $B_1^+$ , and  $PD$  maps from the undersampled data have some artefacts that are predominantly located in the background water.

Figure 2.4 shows the mean estimated  $T_1$  and  $T_2$  values in each sphere of the phantom as a function of their calibrated values for undersampled and fully sampled acquisitions and both estimation methods. The relative differences between mean estimated and calibrated  $T_1$  and  $T_2$  values were respectively below 1.0% and 10.2% for the un-



**Figure 2.3.** Estimated parameter maps in the phantom through dictionary matching and dictionary fitting with both undersampled and fully sampled data. With both the undersampled data (top rows) as the fully sampled data (bottom rows), the dictionary matching maps are closely approximated by the proposed dictionary fitting method while only using 0.03% of the atoms.



**Figure 2.4.** Mean estimated value of  $T_1$  (top) and  $T_2$  (bottom) in each region-of-interest of the phantom as function of their calibrated value (log-log scale). Dictionary fitting obtains for both data sets and each parameter equal accuracy as dictionary matching while using 0.03% of the atoms.

undersampled data, and below 0.7% and 3.1% for the fully sampled data. The root-mean-square error in the  $T_1$  and  $T_2$  estimates was similar for dictionary fitting and dictionary matching (see Supplementary Materials B).

The fitting time was 58 minutes for matching with the densely sampled dictionary while our proposed fitting method with the sparse dictionary took 6 minutes. These times did not include the loading of the dictionaries.

### ***In-vivo Experiment***

Figure 2.5 shows the parameter maps of the in-vivo experiment obtained from fully sampled data using both dictionary matching and dictionary fitting, as well as the difference between their maps. The parameter ranges of  $T_1$  and  $T_2$  are adjusted to highlight the tissues of interest. Differences between the two maps are mostly noticeable around the CSF, and both methods contain some residual structure in the  $B_1$  map.

Compared to maps obtained without SVD compression, dictionary matching had a mean absolute relative error of 0.06% in  $T_1$  and 1.32% in  $T_2$ , while dictionary fitting had an error of 0.15% in  $T_1$  and 2.66% in  $T_2$ . The error of dictionary fitting was somewhat higher than dictionary matching, we hypothesize that the continuous optimization translates variation in the signal (due to the compression) directly to variation in the estimated parameters, while the discrete optimization requires significant

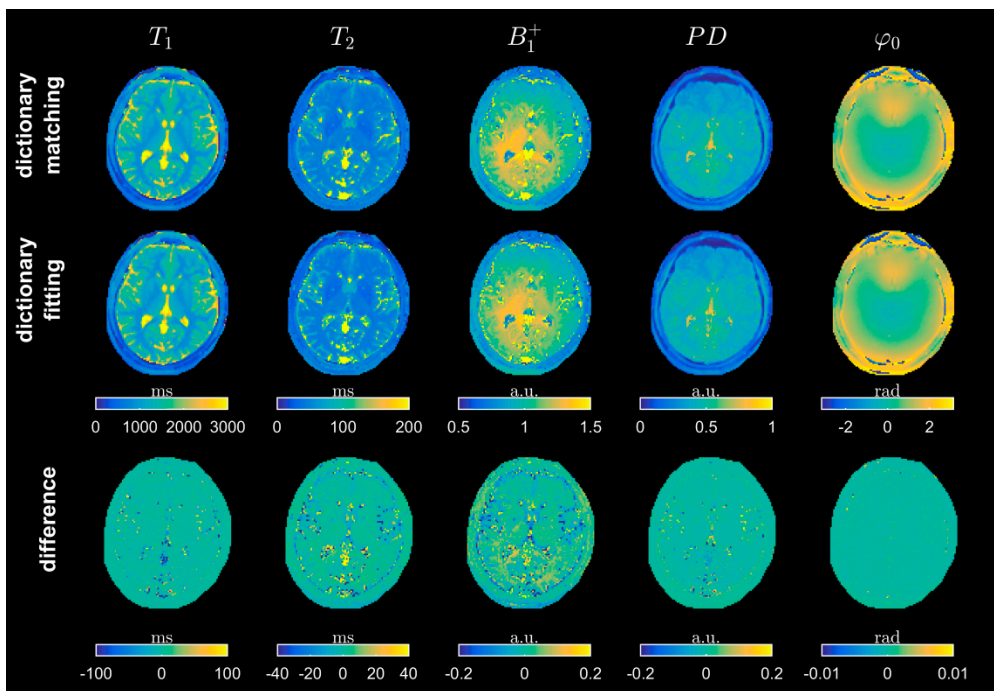


**Figure 2.5.** Parameter maps in the brain from the in-vivo experiment, estimated through dictionary matching (top) and dictionary fitting (middle), and their difference (bottom). Note that the parameter ranges of the difference maps have been adjusted to highlight the differences.

variation in the signal before matching to another element of the dictionary and consequently another discretized parameter value.

The distribution of the error in the  $T_1$  and  $T_2$  maps as function of the number of sampled spirals is shown for both estimation methods in Figure 2.6 (blue and red bars), where the error in each voxel is relative to the value obtained from the fully sampled data with the same estimation method. The proposed method has a smaller spread in error (indicated by the whiskers) than dictionary matching in most maps of each parameter except for the  $T_2$  maps obtained from 1 and 6 spirals. Note that from 6 spirals onwards the dictionary matching approach selected the same atom as the fully sampled reference in the majority of voxels (boxes have zero width) and in most others one step in the dictionary away (whiskers), while the continuous estimate of the proposed fitting approach has a small but finite width. Furthermore, it can be noticed that the relative  $T_1$  error was below the relative  $T_2$  error.

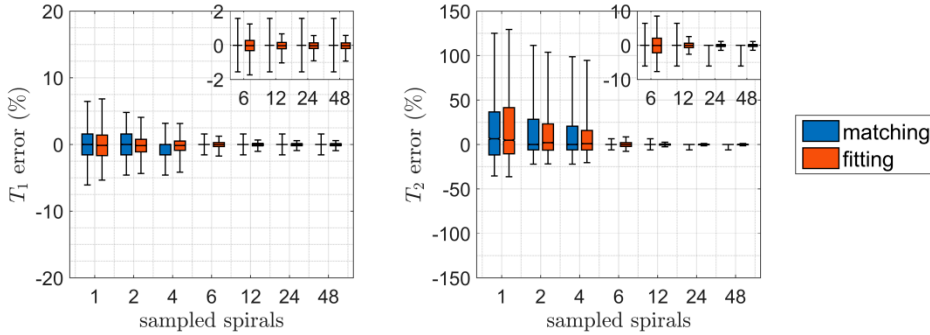


**Figure 2.6.** Box-and-whisker plots of relative difference in  $T_1$  (left) and  $T_2$  (right) parameter values in the brain as function of the number of spirals/interleaves generated by prospective undersampling k-space. Boxes represent 25-75 percentiles and whiskers indicate the 5-95 percentiles of the error values of all voxels in the brain. Both estimation methods have a similar error spread in  $T_1$  and  $T_2$  for each number of sampled spirals.

## Discussion

This chapter presented a novel method for quantitative parameter estimation based on the least-squares fitting of a signal model defined by B-spline interpolation of a sparsely sampled dictionary. The FISP MRF sequence was chosen as the basis imaging sequence due to its ability to estimate multiple parameters simultaneously, though the precision of  $T_1$  appears to be superior to that of  $T_2$  for this sequence [14]. However, the proposed dictionary fitting framework is applicable for general acquisitions and parameters.

The interpolation error was estimated as a function of the parameter resolution for different B-splines orders. With second or third order splines, the resolution of each parameter reduced by approximately an order of magnitude compared to nearest neighbor interpolation. Consequently, the total number of atoms in the dictionary could be reduced with three orders of magnitude, leading to an equal reduction in memory and computational costs while maintaining similar signal accuracy.

The large reduction of resolution of each parameter makes it computationally feasible to estimate an increased number of parameters simultaneously. In Supplementary Materials C, we demonstrated this by constructing and fitting with a five-dimensional dictionary; additionally including intra-voxel dephasing  $T_2'$  and off-resonance frequency  $\Delta\omega_0$ . This only increased the dictionary size by a factor 164 and fitting time by 58.4%. Consequently, the reduced computational and memory costs of dictionary-

based methods enables the development of acquisition schemes that estimate more parameters simultaneously. Furthermore, the accuracy of our model can be increased by extending the Bloch simulation while using similar computing resources for the dictionary generation. Finally, the smaller dictionary sizes benefit methods that require dictionary generation on-the-fly, e.g. to incorporate acquisition details such as movement in the signal model [26].

The interpolation error of the simulated signals was found to be slightly higher than the predetermined threshold at some points near the boundary of the parameter domains. We performed an additional experiment (not shown) with interior points that only require one-dimensional interpolation (i.e. restricting the other two dimensions to the grid), and found that the number of interpolation errors above the threshold reduced to less than 1%, with a maximum of  $6.8 \cdot 10^{-4}$ . This shows that the error is predominantly caused by interpolating in multiple dimensions, while our parameter resolution was based on one-dimensional interpolation. A practical solution would be to set the actually applied threshold somewhat below the preferred accuracy (a factor two is appropriate for our three-dimensional dictionary). Furthermore, we assumed that the interpolation error is maximal near the boundary of the parameter range and Figure 2.2 showed that this was the case for  $T_1$  and  $T_2$ . However, this may not be true for each pulse sequence and for every parameter. Therefore, an evaluation of the interpolation error in the interior of the dictionary is recommended for general application.

The phantom and volunteer experiments showed that the proposed dictionary fitting method was able to estimate  $T_1$  and  $T_2$  with similar accuracy as dictionary matching while reducing the number of atoms three orders of magnitude. The in-vivo  $B_1^+$  maps had residual structure near the CSF, which is probably due to correlation between the  $B_1^+$  and  $T_2$  parameters, which is known for MRF methods [18], [19].

In the presented results, we chose as error threshold  $\alpha = 5 \cdot 10^{-4}$  and assumed that this was sufficiently accurate for errors in the parameters to be dominated by noise (and not e.g. by discretization errors). In Supplementary Materials D, we examined the quality of the in-vivo  $T_1$  and  $T_2$  maps when setting  $\alpha$  a factor 10 higher and lower. This showed that the  $T_1$  maps were reasonably consistent for different  $\alpha$  and B-spline orders  $n \in \{0,1,2,3\}$ . The  $T_2$  maps showed large variation with  $\alpha = 5 \cdot 10^{-3}$ , and small differences around the CSF for  $\alpha = 5 \cdot 10^{-5}$ . Thus, small improvements in  $T_2$  estimation might be possible by lowering the threshold  $\alpha$ . However, we chose not to

do this since the computational and memory requirements of the reference method would be too high for our available resources.

The proposed dictionary fitting method reduced the calculation time of the fit compared to the matching with a dense dictionary. The calculation time of both estimation techniques can be further reduced by parallelizing the fitting over multiple cores. Additionally, the dictionary matching can benefit from smarter search strategies [20], although application to higher dimensions is still limited due to the required dictionary size. The proposed dictionary fitting method used the `trust-region-reflective` algorithm since it was recommended by the MATLAB documentation for constrained optimization with gradients. While we experienced that convergence was reasonably fast, often within 20 iterations, further improvements can likely be found when doing an in-depth analysis of the applied solver. An alternative parameter estimation method is directly fitting the data to the Bloch equations. However, this would require a strong simplification of our signal model as generating only a single atom currently already took 6.10 seconds.

The proposed dictionary fitting method had similar accuracy as a dictionary matching strategy applying a dense dictionary, even when using data with undersampling artifacts. Hence, dictionary fitting is a beneficial substitute in many cases where dictionary matching is currently used. It can be directly inserted in iterative reconstruction methods with undersampled MRF data [26], by replacing the pattern matching with dictionary fitting. Initialization of the fitting through dictionary matching with the sparse dictionary likely enhances the probability of starting the optimization close to the global optimum.

The dictionary fitting framework was presented for a single MRF pulse sequences and associated model parameters, but is easily extendable to other qMRI methods as presented in [9]–[13].

## Conclusion

The Bloch simulated signal is accurately and efficiently approximated through B-spline interpolation of a sparsely sampled dictionary. Therefore, the proposed method enables estimating parameters by fitting a continuous B-spline signal model, which obtains the accuracy of dictionary matching while strongly reducing dictionary size. The required parameter resolution is efficiently determined on the boundary of the

parameter range. The proposed methods were applied to a FISP MRF acquisition in this work, but can be used for any qMRI acquisition scheme.

### **Acknowledgment**

The authors thank Holland PTC for the use of their NIST system phantom.

## Supplementary Materials

### A. Equivalent optimization

Here we show that solution  $\hat{\boldsymbol{\theta}} = \mathbf{f}(\hat{\mathbf{k}})$  of the dictionary matching step in Eq. 2.3 with the condition  $\hat{\rho} = (\mathbf{s}(\hat{\boldsymbol{\theta}})^H \mathbf{m}) / (\mathbf{s}(\hat{\boldsymbol{\theta}})^H \mathbf{s}(\hat{\boldsymbol{\theta}}))$  as given in Eq. 2.4, is also the solution of the optimization in Eq. 2.2 when restricting the search space  $\Theta$  to the parameter combinations in the dictionary. Setting  $\rho = \rho_R + i\rho_I$ , we can write the error term in Eq. 2.2 as function of  $\rho_R, \rho_I \in \mathbb{R}$ :

$$\begin{aligned} \|\mathbf{m} - \rho \mathbf{s}(\boldsymbol{\theta})\|_2^2 &= (\mathbf{m} - \rho \mathbf{s}(\boldsymbol{\theta}))^H (\mathbf{m} - \rho \mathbf{s}(\boldsymbol{\theta})) \\ &= (\bar{\mathbf{m}} - \rho_R \overline{\mathbf{s}(\boldsymbol{\theta})} + i\rho_I \overline{\mathbf{s}(\boldsymbol{\theta})})^T (\mathbf{m} - \rho_R \mathbf{s}(\boldsymbol{\theta}) - i\rho_I \mathbf{s}(\boldsymbol{\theta})) \end{aligned}$$

The bars indicate complex conjugation. Setting the partial derivative with respect to  $\rho_R$  or  $\rho_I$  to zero, gives for both cases Eq. 2.4 as necessary condition for the minimum. With the condition of Eq. 2.4, the error term in Eq. 2.2 can be written as:

$$\begin{aligned} \|\mathbf{m} - \hat{\rho} \mathbf{s}(\boldsymbol{\theta})\|_2^2 &= \|\mathbf{m}\|_2^2 + |\hat{\rho}|^2 \|\mathbf{s}(\boldsymbol{\theta})\|_2^2 - \mathbf{m}^H \hat{\rho} \mathbf{s}(\boldsymbol{\theta}) - \hat{\rho}^H \mathbf{s}(\boldsymbol{\theta})^H \mathbf{m} \\ &= \|\mathbf{m}\|_2^2 + \frac{|\mathbf{s}(\boldsymbol{\theta})^H \mathbf{m}|^2}{\|\mathbf{s}(\boldsymbol{\theta})\|_2^2} - 2 \frac{\mathbf{m}^H \mathbf{s}(\boldsymbol{\theta}) \cdot \mathbf{s}(\boldsymbol{\theta})^H \mathbf{m}}{\|\mathbf{s}(\boldsymbol{\theta})\|_2^2} \\ &= \|\mathbf{m}\|_2^2 - \frac{|\mathbf{m}^H \mathbf{s}(\boldsymbol{\theta})|^2}{\|\mathbf{s}(\boldsymbol{\theta})\|_2^2} \end{aligned}$$

Since  $\mathbf{m}$  is fixed, the minimization in Eq. 2.2 is equal to the maximization in Eq. 2.3 over the discrete parameter values  $\mathbf{f}(\mathbf{k})$ .

### B. Error in $T_1$ and $T_2$ estimates from phantom experiment

Table S2.1 shows the root-mean-square error (RMSE) in the estimated values of  $T_1$  and  $T_2$  from the phantom experiment, relative to their calibrated values. For most cases, the proposed dictionary fitting method reduced the error in the parameter values compared to the reference dictionary matching method. Exceptions were mostly found in the  $T_2$  estimation, where dictionary matching was more accurate than fitting in ROIs 1-3, and more precise in ROIs 7 and 8. The reduced accuracy of the proposed method for high  $T_2$  values (ROIs 1-3) was possibly due to logarithmic spacing of the parameter in the dictionary, leading to large steps between high  $T_2$  values and consequently an inaccurate initialization of the fit. The higher precision of dictionary matching in ROIs 7 and 8 might be due to the matching of the voxels in each ROI to

a discrete set of  $T_2$  values, which can lower the variance if (almost) all voxels are matched to the same parameter value. Overall, the approximation of the signal model through spline interpolation did not increase the error in the estimated  $T_1$  and  $T_2$  compared to dictionary matching.

**Table S2.1.** Root-mean-square error (RMSE) of the estimated  $T_1$  and  $T_2$  values in the voxels of each region-of-interest (ROI) of the phantom with respect to the calibrated value. The error is given as percentage of the calibrated value in each ROI.

ROI	calibrated $T_1$ [ms]	RMSE in $T_1$ [%]				calibrated $T_2$ [ms]	RMSE in $T_2$ [%]			
		undersampled		fully sampled			undersampled		fully sampled	
		matching	fitting	matching	fitting		matching	fitting	matching	fitting
1	<b>2480</b>	1.8	1.1	2.6	2.7	<b>581</b>	31.4	40.8	12.6	15.4
2	<b>2173</b>	3.0	2.7	0.9	0.8	<b>404</b>	42.7	42.7	14.1	15.9
3	<b>1907</b>	2.6	2.6	2.0	1.7	<b>278</b>	17.4	22.3	13.9	15.6
4	<b>1604</b>	3.4	3.2	2.8	2.7	<b>191</b>	34.0	31.2	13.2	12.7
5	<b>1332</b>	3.6	3.1	3.3	3.5	<b>133</b>	52.2	49.9	9.4	7.3
6	<b>1044</b>	4.5	4.3	6.8	6.5	<b>97</b>	32.1	30.8	13.7	14.5
7	<b>802</b>	5.1	5.0	6.6	6.4	<b>64</b>	27.3	31.7	7.9	12.0
8	<b>609</b>	5.5	5.3	5.2	5.2	<b>46</b>	60.2	59.4	9.0	19.1
9	<b>458</b>	7.0	6.7	4.9	4.7	<b>32</b>	40.6	37.5	12.5	10.8
10	<b>337</b>	10.6	10.4	7.9	8.1	<b>23</b>	55.3	51.9	22.6	20.7
11	<b>244</b>	16.6	16.1	9.5	9.3	<b>16</b>	49.6	50.1	29.0	28.2
12	<b>177</b>	53.6	52.6	48.3	48.2	<b>11</b>	395.3	418.0	393.2	396.7
13	<b>127</b>	22.1	22.1	14.2	15.1	<b>8</b>	78.3	79.8	49.6	51.5
14	<b>91</b>	27.6	26.8	16.0	16.3	<b>6</b>	147.7	156.0	65.8	64.2

### C. Higher dimensional parameter estimation

Here we show that dictionary fitting enables the estimation of an increased number of parameters compared to dictionary matching. We added estimation of intra-voxel dephasing of spins  $T'_2$  and static field inhomogeneity  $\Delta B_0$  from the in-vivo scan, and consequently increased the dimensionality of our dictionary from three to five. The number of spins used in our model is increased by a factor 10 in order to accurately model the intra-voxel dephasing.

Figure S2.1 shows the number of discretized values in each parameter dimension for B-spline orders  $n = 0, 1, 2, 3$ , as determined through the method described in Section “Parameter Resolution”. The interpolation error in the  $T'_2$  and  $\Delta\omega_0$  dimension converged to a value just below the target error. We found (data not shown) that the minimal interpolation error in these dimensions scaled with the square root of the number

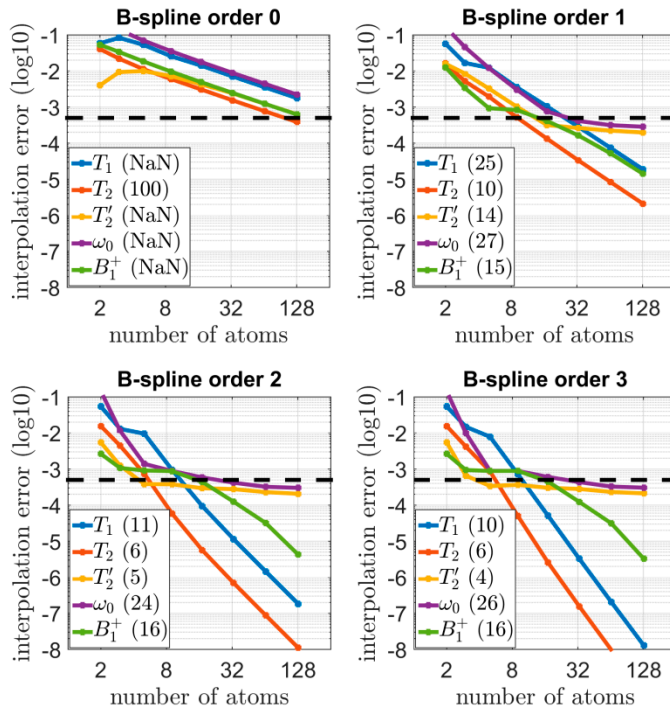


**Figure S2.1.** Interpolation error on the edge of parameter space as function of number of atoms in each dimension. Dashed line indicates target error and the legend shows for each parameter the minimum number of atoms required to obtain the target error. Note that for B-spline order  $n = 0$ , the target interpolation error is only obtained in the  $T_2$  dimension with less than 130 atoms.

of spins used in the simulations. Dictionary fitting (Eq. 2.8) was done with B-spline order  $n = 2$ , using a dictionary with 11, 6, 5, 24, and 16 parameter values in respectively the ranges of  $T_1, T_2, T_2', \Delta\omega_0$ , and  $B_1^+$ . Storage of this dictionary required 2,34 GB without SVD and 74,1 MB when projected on the first 30 singular vectors, a factor 164 increase compared to the three-dimensional dictionary. Fitting the in-vivo maps with the SVD-projected dictionaries took 301 seconds which is 58,4% longer than the fitting time using the three-dimensional dictionary.

Figure S2.2 shows the parameter maps obtained from fitting with a dictionary with five parameter dimensions. The  $T_2'$  parameter map obtained with the five-dimensional dictionary looks implausible, which is expected since the used acquisition is typically not used to estimate this parameter. The  $\Delta\omega_0$  map shows some off-resonance around the sinuses which is likely due to the air-tissue interface, even though the applied acquisition is designed to be robust against off-resonance effects. The low signal region

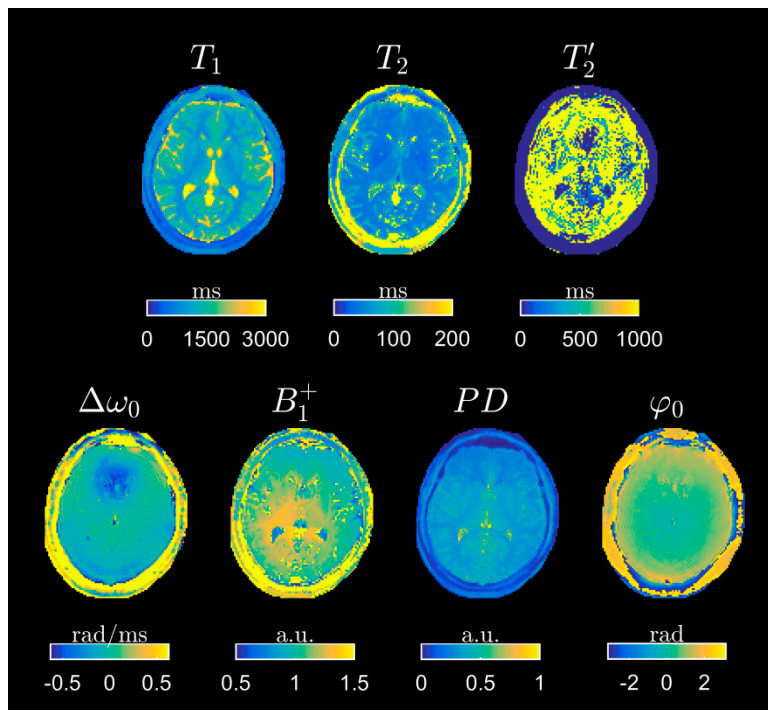


**Figure S2.2.** Parameter maps in the brain from dictionary fitting with B-spline order  $n = 2$  using a five-dimensional dictionary. Although the  $T_2'$  and  $\Delta\omega_0$  maps have low quality, this example shows that the proposed method is computationally feasible for seven-dimensional parameter estimation.

near the skull leads to the mapping of very low  $T_2'$  values which also led to implausible values of  $T_2$ ,  $\Delta\omega_0$ , and  $B_1^+$ .

Although for the evaluated FISP MRF acquisition the additional parameter maps were either implausible ( $T_2'$ ) or typically irrelevant ( $\Delta\omega_0$ ), we have shown that the dictionary fitting method is able to estimate seven parameters simultaneously, using a five-dimensional dictionary. If we suppose that for B-spline order  $n = 0$ , the target interpolation error in Figure S2.1 is obtained using 129 atoms for  $T_1, T_2', \omega_0$  and  $B_1^+$ , then matching with a dictionary that obtains the target interpolation error would require 189 TB storage for the dictionary (without SVD), and  $4.8 \cdot 10^7 (= 100 \cdot 129^4 \cdot \frac{6.2}{3600})$  computer hours to generate (with the used Bloch simulation that requires on average 6.2 s per atom). The proposed method enables the design of new quantitative acquisitions that can estimate an increased number of parameters simultaneously and consequently obtain more biomarkers (e.g.  $T_1, T_2, T_2', PD$ ) with reduced bias due to the magnetic fields ( $\Delta\omega_0, B_1^+, \varphi_0$ ).

### D. Effect of B-spline Order and Interpolation Accuracy

Here we present a qualitative comparison of the  $T_1$  and  $T_2$  parameter maps obtained through dictionary fitting with different combinations of B-spline order  $n \in \{0,1,2,3\}$  and interpolation accuracy  $\alpha \in \{5 \cdot 10^{-3}, 5 \cdot 10^{-4}, 5 \cdot 10^{-5}\}$ . For each combination, we generated a dictionary with parameter resolution as predicted by the methods described in Section “Parameter Resolution” (i.e. by shifting the threshold in each graph of Fig. 1). The resulting parameter resolutions are shown in Table S2.2. The combination  $n = 0$  with  $\alpha = 5 \cdot 10^{-5}$  was excluded since it required more than the maximal number (512) of atoms in each parameter dimension. This would require more than a TB memory for dictionary storage, which is unfeasible for our available resources.

Fig. S2.3 shows the  $T_1$  maps from dictionary fitting with each combination of B-spline order  $n$  and interpolation threshold  $\alpha$ . The different  $T_1$  maps appear reasonably consistent, except for  $n = 0$  with  $\alpha = 5 \cdot 10^{-3}$  where some quantization error is observable. Fig. S2.4 contains the  $T_2$  maps from the same combinations of  $n$  and  $\alpha$ . Here, the differences between the maps are larger. There is a large variation between the  $T_2$  maps with interpolation error  $\alpha = 5 \cdot 10^{-3}$ , which suggests that this error threshold is too high for reliably estimating this parameter. The maps with threshold  $\alpha = 5 \cdot 10^{-4}$  and  $\alpha = 5 \cdot 10^{-5}$  are more consistent and only show some slight variation around the CSF.

**Table S2.2.** Estimated number of atoms required in each parameter dimension to obtain a given interpolation accuracy  $\alpha$  using B-spline order  $n$ . These numbers were estimated as described in “Parameter Resolution” Section.

	$n = 0$			$n = 1$			$n = 2$			$n = 3$		
	$T_1$	$T_2$	$B_1^+$									
$\alpha = 5 \cdot 10^{-3}$	47	11	17	8	3	2	6	3	2	6	3	2
$\alpha = 5 \cdot 10^{-4}$	454	97	160	25	10	17	11	6	18	10	6	18
$\alpha = 5 \cdot 10^{-5}$	> 512			80	27	98	21	10	78	18	9	77

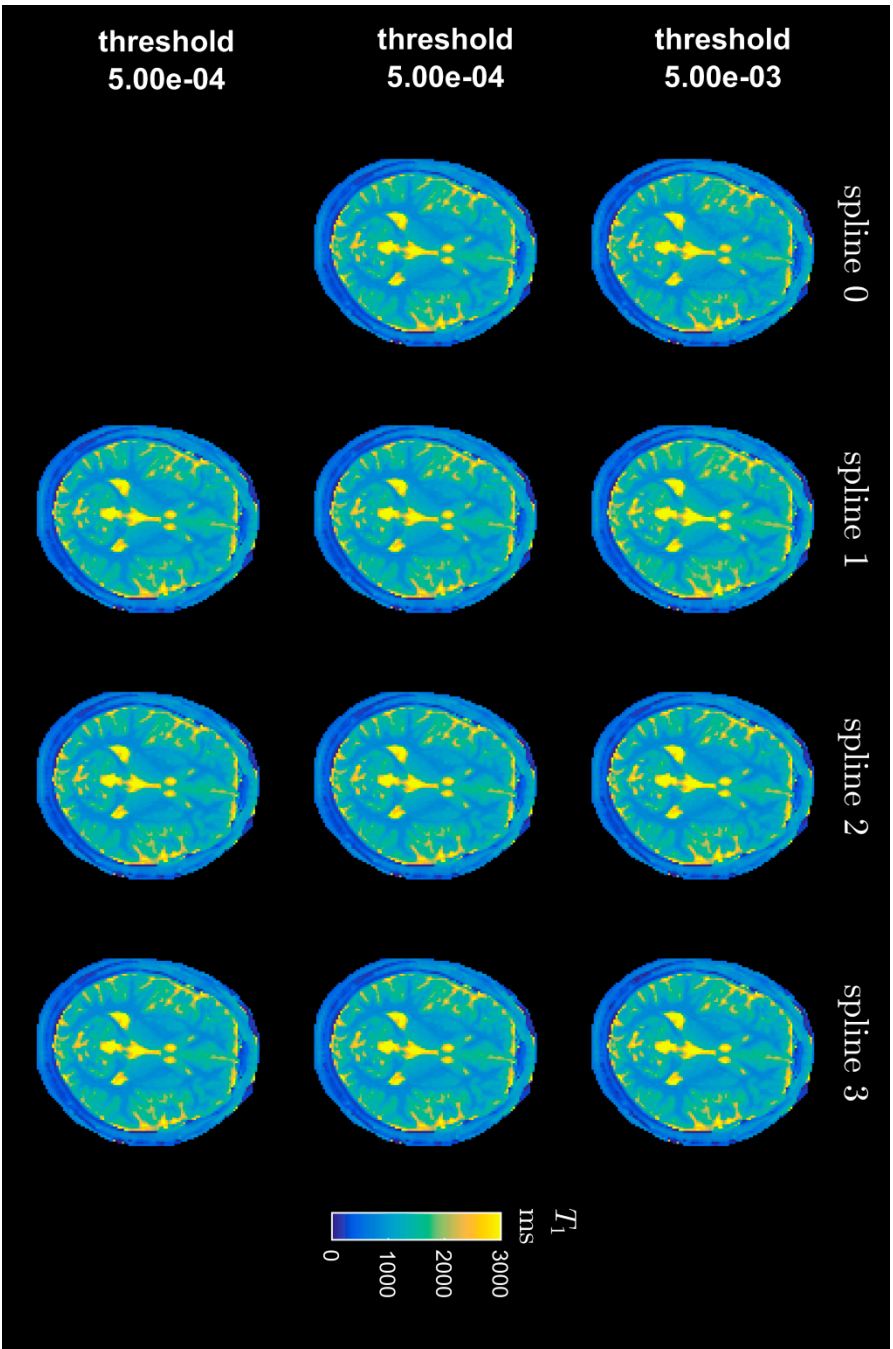


**Figure S2.3.** Parameter maps of  $T_1$  in the brain for B-spline orders  $n = 0, 1, 2, 3$  (columns) and for each B-spline order multiple levels of interpolation accuracy  $\alpha$ . The combination  $n = 0$  and  $\alpha = 5 \cdot 10^{-4}$  was not included since the required dictionary size was too large for our available resources.

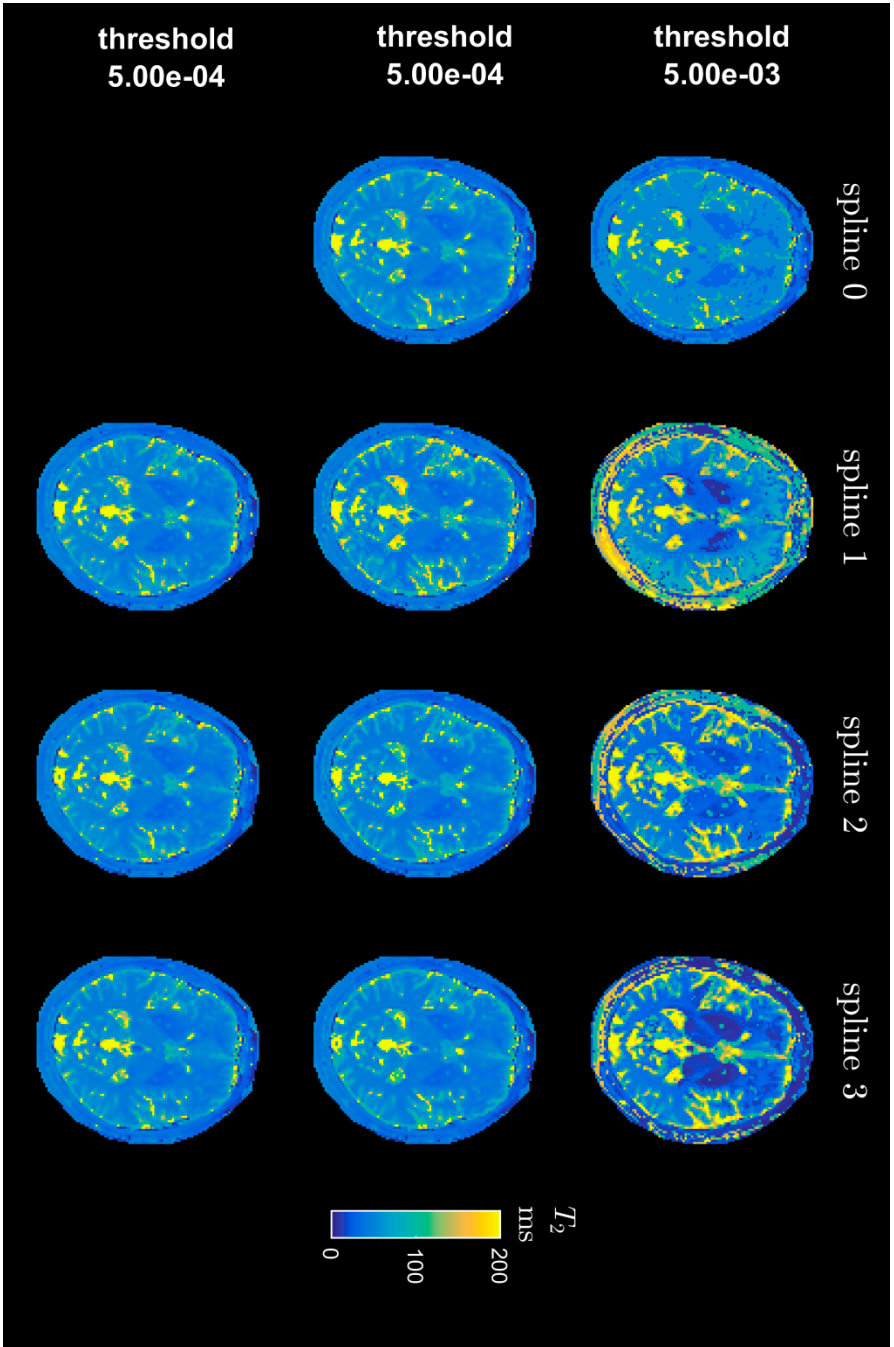


**Figure S2.4.** Parameter maps of  $T_2$  in the brain for B-spline orders  $n = 0, 1, 2, 3$  (columns) and for each B-spline order multiple levels of interpolation accuracy  $\alpha$ . The combination  $n = 0$  and  $\alpha = 5 \cdot 10^{-4}$  was not included since the required dictionary size was too large for our available resources.

# Time Efficiency

# Determining the Time Efficiency of Quantitative MRI Methods through a General Framework based on Bloch Simulations

Willem van Valenberg, Frans M. Vos, Stefan Klein, Lucas J. van Vliet, Dirk H.J. Poot

## Abstract

This work aims to enable an objective comparison between quantitative MRI (qMRI) methods based on their time efficiency: the expected precision of each parameter estimate (e.g.  $T_1, T_2$ ) within a fixed scan time. The comparison can be made in-silico and consequently avoids costly evaluations of each method on the scanner.

The expected precisions were determined from simulations of the MR signal through the Cramér-Rao lower bound theorem. The signal was modelled using the Bloch equations, which is applicable to any qMRI method and consequently enables the comparison of their precisions within a common framework. The framework was applied to nine established qMRI methods for which we predicted the time efficiency values of seven parameters ( $T_1, T_2, T_2^*, PD, \varphi_0, \Delta B_0, B_1^+$ ). The predicted time efficiency values were compared for parameter values corresponding to white matter and muscle tissue. Finally, the framework was validated by comparing the predicted precisions to the measured standard deviations in the NIST system phantom.

Each qMRI method had high time efficiency values for estimating the parameters it is conventionally associated with. The phantom experiment showed that the measured precision of each parameter was accurately predicted by our framework for most qMRI methods. Out of a 672 cases, the measured precision was lower than predicted in only 94 (12.4%) cases. In all other cases, high predicted precision was matched with high measured precision.

The presented framework provides time efficiency values that closely match the precision per unit scan time, and as such enables an objective in-silico comparison of qMRI methods.

## Introduction

Quantitative MRI (qMRI) methods estimate the physical parameters underlying the MR signal in order to increase the specificity and reproducibility of the acquired data compared to conventional MR imaging. These parameters can describe processes such as magnetization relaxation, water diffusion, blood perfusion, oxygen consumption, magnetization transfer, and others (see [27] for a comprehensive overview). Each parameter can often be estimated with multiple methods that differ in accuracy (i.e. bias), precision (estimation variance), acquisition time, and other features such as motion sensitivity, gating capabilities and/or fat suppression. Consequently, selecting the best qMRI method for parameter estimation is problematic. While each feature is relevant, we consider the precision to have the most direct link to the reproducibility of the parameter estimates. Therefore, we aim to facilitate method selection by comparing the precision of qMRI methods.

A number of practical requirements can be defined for measuring the precision of qMRI methods. First, the measure should account for differences in scan time, since every method becomes more precise by averaging over repeated measurements at the expense of increased scan time. Second, it should be based on the estimation of a consistent set of parameters, since the fixation of any parameter can increase the precisions of the estimates at the cost of (potential) bias. Finally, the measure should avoid time-consuming evaluation of each qMRI method on the scanner, which can be prohibitively expensive when taking the full range of possible tissues and acquisition settings into account. Therefore we aim to define a measure of the precision that is 1) normalized for the acquisition time, 2) based on a consistent set of parameters, and 3) evaluated in-silico, in order to enable an objective comparison of qMRI methods.

The precision of a qMRI method can be theoretically estimated from its signal model and the (estimated) noise level through the Cramér-Rao lower bound (CRLB) theorem [28]. We define the *time efficiency* of a qMRI method as the CRLB-derived precision normalized by the acquisition time. As such, time efficiency is independent on the number of averages, and the qMRI method with the highest time efficiency obtains the most precise parameter estimate in a given scan time.

In-silico estimates of the precision (or SNR) normalized by scan time have previously been used to compare methods for  $T_1$ -weighted imaging [29], and for  $T_1$  and  $T_2$  map-

ping [30], [31]. However, the methods in these comparisons are described by different signal models with varying underlying assumptions (e.g. homogeneous magnetic fields and complete signal spoiling). Consequently, the results depend on these assumptions and may be invalid when there are imperfections in the scanning system. An objective comparison of the time efficiency of qMRI methods requires the estimation of a common set of parameters through a shared signal model.

In this paper, we present and validate a new framework for comparing the time efficiency of qMRI methods. The framework determines the CRLB through Bloch simulations of the MR signal, which are applicable to any pulse sequence and can describe most of the relevant physics. We evaluate the framework by determining the time efficiency of methods that estimate seven parameters: proton density ( $PD$ ), longitudinal relaxation time ( $T_1$ ), transversal relaxation time ( $T_2$ ), apparent transversal relaxation time ( $T_2^*$ ), the off-resonance ( $\Delta B_0$ ) field, RF transmit ( $B_1^+$ ) field, and transmit-receive phase ( $\varphi_0$ ). Multiple methods are selected that are conventionally used in literature, and each is implemented using the TOPPE framework [32] to enable equal acquisition settings (e.g. resolution, field-of-view, slice width). We show that the CRLB-predicted precision is matched by the precision obtained from measurements for most qMRI methods. This makes time efficiency a promising measure for the selection and optimization of qMRI methods.

## Theory

The proposed time efficiency framework is presented for a general qMRI method that estimates  $P$  parameters from  $M$  measurements of the complex-valued MR signal  $\mathbf{m} \in \mathbb{C}^M$  in a voxel. The parameters  $\boldsymbol{\theta} \in \mathbb{R}^P$  in each voxel are mapped to the signal through the model  $\mathbf{s}(\boldsymbol{\theta}) \in \mathbb{C}^M$ . In the experiment section, our focus will be on  $P = 7$  parameters ( $T_1, T_2, T_2^*, PD, \varphi_0, \Delta B_0, B_1^+$ ) for which a signal is modeled/generated based on Bloch simulations. However, the presented time efficiency framework is applicable to other combinations of parameters and/or signal models as well.

### **Precision Estimation**

The measured MR signal  $\mathbf{m} \in \mathbb{C}^M$  contains Gaussian noise and is therefore a noisy realization from a multivariate, normal probability distribution around the (assumed) true signal  $\mathbf{s}(\boldsymbol{\theta})$ . Conversely, this multivariate distribution can be considered a likelihood function of parameters  $\boldsymbol{\theta}$  for given samples  $\mathbf{m}$ . The likelihood function is com-

monly used to quantify the amount of information the signal contains about  $\boldsymbol{\theta}$  through the Fisher information matrix [28]. Assuming that the noise on the samples is uncorrelated and identically distributed with variance  $\sigma^2 \in \mathbb{R}$ , the Fisher information matrix equals:

$$\mathbf{I}(\boldsymbol{\theta}) = \frac{1}{\sigma^2} \left( \frac{\partial \mathbf{s}(\boldsymbol{\theta})}{\partial \boldsymbol{\theta}} \right)^H \left( \frac{\partial \mathbf{s}(\boldsymbol{\theta})}{\partial \boldsymbol{\theta}} \right) \in \mathbb{R}^{P \times P}. \quad (3.1)$$

Here,  $H$  indicates the Hermitian conjugate. The determination of the derivative of  $\mathbf{s}(\boldsymbol{\theta})$  will be detailed later (see Signal Model).

The Cramér-Rao lower bound (CRLB) theorem states that  $\mathbf{I}(\boldsymbol{\theta})^{-1}$  is a lower bound on the covariance matrix of any set of unbiased estimators of  $\boldsymbol{\theta}$  [28]. Specifically, the diagonal elements of  $\mathbf{I}(\boldsymbol{\theta})^{-1}$  are lower bounds on the variance of estimates of the different parameters  $\boldsymbol{\theta}$ . If we assume that there is an estimator that attains the CRLB, we can thus theoretically estimate the precision of a qMRI method based on the signal model  $\mathbf{s}(\boldsymbol{\theta})$  and the (expected) noise level  $\sigma$ . Previous work applied the CRLB for the optimization of acquisition settings in a wide range of qMRI applications such as relaxometry [33]–[41], diffusion [42]–[44], kinetic modelling [45], magnetization transfer [46], [47], water/fat-decomposition [48], and temperature measurement [49].

### ***Time Efficiency***

The CRLB has two issues when used as a tool to compare the precision of qMRI methods. First, the precision (i.e. the reciprocal of the variance) scales linearly with the number of averages/repeats of a method, and consequently with its scan time  $T_{acq}$ . To compensate for this effect we define a preferred scan time  $T_{ref}$ , constant for all methods, and scale the precision of each method by the (relative) number of averages  $N_{avg} = T_{ref}/T_{acq}$ . Second, the matrix inversion of  $\mathbf{I}(\boldsymbol{\theta})$  might be ill-conditioned or even degenerate when  $\mathbf{m}$  contains (almost) no information on a specific parameter. To ensure invertibility we add a positive definite matrix  $\mathbf{P} \in \mathbb{R}^{P \times P}$  that can be interpreted as the inverse covariance matrix of an assumed Gaussian prior on  $\boldsymbol{\theta}$ .

Hence, we define a modified information matrix:

$$\bar{\mathbf{I}}(\boldsymbol{\theta}) := \mathbf{I}(\boldsymbol{\theta}) N_{avg} + \mathbf{P} \quad (3.2)$$

By virtue of the CRLB,  $\bar{\mathbf{I}}(\boldsymbol{\theta})^{-1}$  is a lower bound on the variance that can be obtained in a scan time  $T_{ref}$ . Next, we define the reciprocal of the diagonal elements of  $\bar{\mathbf{I}}(\boldsymbol{\theta})^{-1}$ , i.e. the variances of the parameters, as time efficiency,  $\mathbf{E}(\boldsymbol{\theta}) \in \mathbb{R}^P$ , of a qMRI method:

$$E_p(\boldsymbol{\theta}) := \frac{1}{(\bar{\mathbf{I}}(\boldsymbol{\theta})^{-1})_{p,p}} \in \mathbb{R}, \quad \text{for } p \in \{1, 2, \dots, P\} \quad (3.3)$$

Note that  $E_p(\boldsymbol{\theta}) \leq \bar{I}_{p,p}(\boldsymbol{\theta})$  for each parameter  $\theta_p$ , where equality is only attained if the information on parameter  $\theta_p$  is orthogonal to the other parameters:  $\bar{I}_{p,q}(\boldsymbol{\theta}) = 0$  if  $p \neq q$ . Differences between  $\bar{I}_{p,p}(\boldsymbol{\theta})$  and  $E_p(\boldsymbol{\theta})$  are due to the influence of the other parameters (confounds) on the information in parameter  $\theta_p$ . The time efficiency  $\mathbf{E}(\boldsymbol{\theta})$  of a given qMRI method depends on the noise level  $\sigma$  which varies between experiments. However, this dependence is almost linear (with the exception of the prior), so relative differences in time efficiency between qMRI methods should be consistent between experiments.

In order to compare the information  $\bar{I}(\boldsymbol{\theta})_{p,p}$  or time efficiency  $E_p(\boldsymbol{\theta})$  of a qMRI method for different parameters, we define the signal-to-noise ratio of a parameter, relative to a reference value  $\theta_p^{ref}$ , as:

$$\begin{aligned} SNR_p^I &:= \theta_p^{ref} \cdot \sqrt{\bar{I}(\boldsymbol{\theta})_{p,p}} \\ SNR_p^E &:= \theta_p^{ref} \cdot \sqrt{E_p(\boldsymbol{\theta})} \end{aligned} \quad \text{for } p \in \{1, 2, \dots, P\}, \quad (3.4)$$

where  $SNR_p^I$  and  $SNR_p^E$  can be conceived as the signal-to-noise ratio when the other parameters are assumed to be known and unknown respectively. Observe that  $SNR_p^I$  and  $SNR_p^E$  are essentially reciprocal of the theoretical coefficients-of-variation.

## Methods

The time efficiency  $\mathbf{E}(\boldsymbol{\theta})$  was designed to be informative for sequence selection and predictive of the parameter precision obtained in practice. We evaluated this by comparing and validating the time efficiency values of nine established qMRI methods for the estimation of  $P = 7$  parameters  $\boldsymbol{\theta} = (T_1, T_2, T_2^*, PD, \varphi_0, \Delta B_0, B_1^+)$ . Table 3.1 lists the nine qMRI methods used in our experiments with relevant acquisition settings

that approximate literature references [11], [14], [50]–[55]. The shown scan times were based on the experimental settings (e.g. readout bandwidth, resolution) used in the validation experiment (see Phantom Study).

Clearly, certain parameters cannot be reliably estimated with particular methods. While qMRI methods usually consider one or multiple of these parameters to be constant, or assume that they have zero effect on the contrast differences, we included the effect of all parameters in a single signal model and push the solution of the parameter estimation to reasonable values by assuming some prior knowledge on the distribution of each parameter (see Parameter Estimation).

**Table 3.1.** Overview of qMRI methods, related parameters, used settings, literature reference, and scan time ( $T_{acq}$ ). The methods are: Inversion-Recovery Look-Locker (IRLL), Inversion-Recovery Spin-Echo (IRSE), Variable Flip Angle SPGR (VFA), Bloch-Siegert (BS), Multiple Gradient-Echo (MGE), Spin-echo (SE), Multiple Spin-Echo (MSE), and Magnetic Resonance Fingerprinting (MRF). Settings include flip angle ( $FA$ ), number of measurements ( $N$ ), repetition time ( $T_R$ ), inversion time ( $T_I$ ), echo time ( $T_E$ ), and echo spacing ( $ESP$ ). The scan time  $T_{acq}$  is given for a 2D acquisition that samples 200 k-space lines and where each steady-state is measured with a minimal of 5 s preparation after a 5 s delay from the previous measurement.

Method	Parameter	Settings	Ref	$T_{acq}$ (min:s)
IRLL	$T_1$	$FA = 20^\circ, N = 16, T_I = 10$ ms, $ESP = 75$ ms, $T_E = 3.2$ ms, $T_R = 1220$ ms, RF spoiling	[50]	4:16
IRSE	$T_1$	$T_I = [30, 530, 1030, 1530]$ ms, $T_R = 1600$ ms, $T_E = 15$ ms,	[51]	22:06
VFA	$T_1$	$FA = [5, 10, 15, 20, 25]^\circ, T_R = 9$ ms, $T_E = 3.2$ ms, RF spoiling	[52]	1:00
VFA + BS	$T_1, B_1^+$	combination of the specified VFA and BS methods		2:00
BS	$B_1^+$	BS with settings: $FA = 20^\circ, T_R = 100$ ms, $T_E = 20$ ms, 10 ms Fermi pulse with $\pm 4$ kHz off-resonance, RF spoiling	[53]	1:00
MGE	$T_2^*$	$N = 32, ESP = 5$ ms, $FA = 30^\circ, T_R = 700$ ms	[54]	2:31
SE	$T_2$	$T_E = [15, 30, 60, 120, 240]$ ms, $T_R - T_E = 1500$ ms	[55]	27:29
MSE	$T_2$	$N = 16, ESP = 15$ ms, $T_R = 2500$ ms	[11]	8:30
MRF	$T_1, T_2, B_1^+$	$N = 1000, FA \in [0, 70]^\circ, ESP \in [11.5, 14.5]$ ms, $T_E = 3.5$ ms, $T_R = 13$ s, gradient spoiling	[14]	44:19

### Signal Model

The signal function  $\mathbf{s}(\boldsymbol{\theta})$  of each qMRI method in Table 3.1 was constructed using an event-based Bloch simulator that combines the waveforms and signal readout times of each qMRI method into a single ordered sequence. The computational complexity of the simulation was reduced by modelling the radiofrequency pulses and gradient waveforms as a small number of hard (instantaneous) pulses and ignoring the k-space trajectory. As such the signal was simulated in a single voxel. Such single voxel simulation enables to study the ‘pure’ efficiency of the qMRI methods and to exclude the influence of different k-space samplings. In order to accurately model the intra-voxel dephasing, we simulated and integrated over approximately  $10^6$  spins with off-resonance frequencies that are Cauchy distributed around  $\gamma\Delta B_0$  with scale  $T_2'^{-1} = T_2^{*-1} - T_2^{-1}$ . Furthermore, the spins were spatially distributed over twice the desired slice width (5 mm) to model the slice selective excitation and refocusing pulses. Due to the slice selective excitation, the maximal signal strength is 50% of  $PD$ . Each simulation was initialized by repeating the sequence for an acquisition time of at least 5 seconds. This ensures approximation to the pseudo steady-state within 5% for a maximal  $T_1$  of 1669 ms. To construct  $\mathbf{s}(\boldsymbol{\theta})$  for combined methods (VFA+BS) the signal model  $\mathbf{s}(\boldsymbol{\theta})$  and measurements  $\mathbf{m}$  of the separate acquisitions were concatenated.

The described Bloch simulations have a high computational complexity due to the large number of spins and discretized time steps. This makes conventional iterative optimization methods for parameter estimation infeasible due to the repeated evaluation of the model. Therefore, we approximated  $\mathbf{s}(\boldsymbol{\theta})$  for  $\boldsymbol{\theta} \in \Theta \subset \mathbb{R}^7$  by a signal model  $\tilde{\mathbf{s}}(\boldsymbol{\theta})$  defined through a dictionary interpolation approach [56]. The dictionary contains the Bloch-simulated signals from a coarse, uniform grid of parameter combinations, and was evaluated once for each qMRI method. Subsequently, the signal model  $\tilde{\mathbf{s}}(\boldsymbol{\theta})$  was defined for  $\boldsymbol{\theta} \in \Theta \subset \mathbb{R}^7$  through second-order B-spline interpolation between signals in the dictionary (i.e. by using the grid of parameter combinations as knot points). Both the interpolant  $\tilde{\mathbf{s}}(\boldsymbol{\theta})$  as its derivative can be determined efficiently [24], which enabled the use of iterative methods for parameter estimation. Furthermore, we determined the Fischer Information in Eq. 3.1 using the derivative of  $\tilde{\mathbf{s}}(\boldsymbol{\theta})$  in order to avoid the choice of step size for a numerical derivative of  $\mathbf{s}(\boldsymbol{\theta})$ .

Table 3.2 lists the domain of each parameter and the sampling strategy of the knot points (linearly or logarithmically). The parameter resolution (see Supporting Table

**Table 3.2.** Discretized parameters in the applied dictionary with their domain, sampling strategy, and the mean and standard deviation (std) of the Gaussian prior used for parameter estimation. Note that  $T_2^{*-1} = T_2^{-1} + T_2'^{-1}$ .

symbol	name	domain	unit	sampling strategy	prior	
					mean	std
$T_1$	longitudinal relaxation	[5, 6000]	ms	log	log(100)	log(100)
$T_2$	transversal relaxation	[5, 2000]	ms	log	log(50)	log(100)
$T_2'$	intra-voxel dephasing	[10, 1000]	ms	log	log(50)	log(100)
$\Delta B_0$	static field inhomogeneity	$[-2\pi/10, 2\pi/10]$	rad/ms	linear	0	1
$B_1^+$	transmit field inhomogeneity	[0.5, 1.5]	a.u.	linear	1	0.5

S3.1) was set to obtain a maximum of  $10^{-3}$  interpolation error between the knot points, while adopting  $PD = 1$ . Note that the parameters  $PD$  and  $\varphi_0$  were not discretized since they are determined directly from the scale and phase difference between measurements and fitted model (see below). Furthermore, the value of  $T_2^*$  is not estimated directly, but set to  $T_2^{*-1} = T_2^{-1} + T_2'^{-1}$ .

### Parameter Estimation

Parameter estimation was initialized at the dictionary atom that maximized the norm of the inner product with the acquired signal over all atoms for which  $\Delta B_0 = 0$  and  $B_1^+ = 1$ . Subsequently, we determined the maximum a posteriori estimate  $\hat{\theta} \in \mathbb{R}^7$  from the measurements  $\mathbf{m}$ , through the least squares fitting:

$$\hat{\theta} = \arg \min_{\theta \in \Theta \subset \mathbb{R}^7} \frac{\|\mathbf{m} - \tilde{\mathbf{s}}(\theta)\|_2^2}{\sigma^2} + (\theta - \theta_{\text{prior}})^T \mathbf{P} (\theta - \theta_{\text{prior}}) \quad (3.5)$$

in which  $\sigma^2$  equals the (estimated) noise variance. Vector  $\theta_{\text{prior}}$  indicates the mean of the prior distribution and  $\mathbf{P}^{-1}$  is its (diagonal) covariance matrix. Parameters  $T_1, T_2, T_2', \Delta B_0, B_1^+$  have their mean and variance of the prior specified in Table 3.2, and for  $PD$  and  $\varphi_0$  we do not apply a prior (i.e.  $P_{i,i} = 0$ ). Note that the prior applies to the log-time values of the relaxometry parameters, such that the standard deviation reflect two orders of magnitude difference from the mean values. The fitting was im-

plemented using the `fmincon` routine from MATLAB (The Mathworks, Natick, MA) with the `trust-region-reflective` algorithm which was stopped after 500 iterations or when the relative improvement in subsequent steps was below  $10^{-6}$ .

### **Simulation Study**

The time efficiency framework was first evaluated for the qMRI methods in Table 1 with two example tissues: white matter ( $T_1/T_2 = 1084/69$  ms) and muscle tissue ( $T_1/T_2 = 1412/50$  ms). The  $T_1$  and  $T_2$  values were taken from [57]; for the other parameters in  $\theta$  we chose:  $T_2' = 200$  ms,  $PD = 1$ ,  $\varphi_0 = 0$  rad,  $\Delta B_0 = 0$  rad/ms, and  $B_1^+ = 1$ . The noise level was set to obtain approximately the same  $PD$ -to- $\sigma$  ratio as obtained in the subsequent phantom study. For each estimated parameter of each qMRI method,  $SNR_p^I$  and  $SNR_p^E$  were determined through Eq. 3.4, with reference parameter  $\theta_p^{ref}$  equal to  $2\pi/1000 \frac{\text{rad}}{\text{ms}} = 1$  Hz for  $\Delta B_0$ , 1 rad for  $\varphi_0$ , and the previously defined input value  $\theta_p$  for  $T_1, T_2, T_2^*, B_1^+$  and  $PD$ .

### **Phantom Study**

The time efficiencies of the qMRI methods in Table 1 were experimentally assessed on a 3.0-T Discovery system (GE Healthcare) using the NIST system phantom [25]. With each qMRI method we acquired the same 2D slice that intersected 14 spheres with calibrated  $T_1$  and  $T_2$  values. This was done twice for each qMRI method such that the variance in each parameter could be estimated from the difference map. Common scan properties of the methods were:  $200 \times 200$  Cartesian matrix,  $\pm 62.5$  kHz bandwidth,  $1 \times 1$  mm<sup>2</sup> FOV, and a slice thickness of 5 mm. To enable strict control over implementation and settings, we implemented each qMRI method using the TOPPE framework [32] (see Supporting Information for implementation details). We publicly provide the TOPPE sequence files on [https://bitbucket.org/big\\_erasmusmc/time-efficiency](https://bitbucket.org/big_erasmusmc/time-efficiency).

A region-of-interest (ROI) was manually drawn inside each of the 14 spheres. In every ROI, we estimated the parameters  $\hat{\theta} \in \mathbb{R}^7$  in each voxel through Eq. 3.5 for both repeats of a qMRI method. Subsequently, we determined the difference of each estimated parameter  $\hat{\theta}_p$  between repeats, and set the measured standard deviation  $\sigma_{p,meas}$  equal to the standard deviation of the difference across the voxels of the ROI divided by  $\sqrt{2}$ . Assuming that the estimated parameters are normally distributed, the 95% confidence interval of the true standard deviation of each parameter equals

$\left[ \sqrt{\frac{N_{ROI}-1}{\chi_{0.025}^2}} \sigma_{p,meas}, \sqrt{\frac{N_{ROI}-1}{\chi_{0.975}^2}} \sigma_{p,meas} \right]$ , where  $N_{ROI}$  is the number of voxels in a ROI and  $\chi_{\alpha}^2$  is the  $\alpha$ -th quantile of the chi-square distribution with  $N_{ROI} - 1$  degrees of freedom.

The observed precision was compared to the theoretically expected standard deviation  $\sqrt{1/E_p(\boldsymbol{\theta})}$  with  $N_{acq} = 1$  for each method, where  $\boldsymbol{\theta}$  contained the calibrated  $T_1$  and  $T_2$  values,  $T_2' = 200$  ms,  $PD = 1$ ,  $\varphi_0 = 0$  rad. For  $\Delta B_0$  and  $B_1^+$  we used the values estimated by respectively the MGE and BS methods.

## Results

### Simulation Study

Figure 3.1 shows the SNR predictions for all parameters per qMRI method for white matter and muscle tissues respectively. The white and colored bars denote respectively

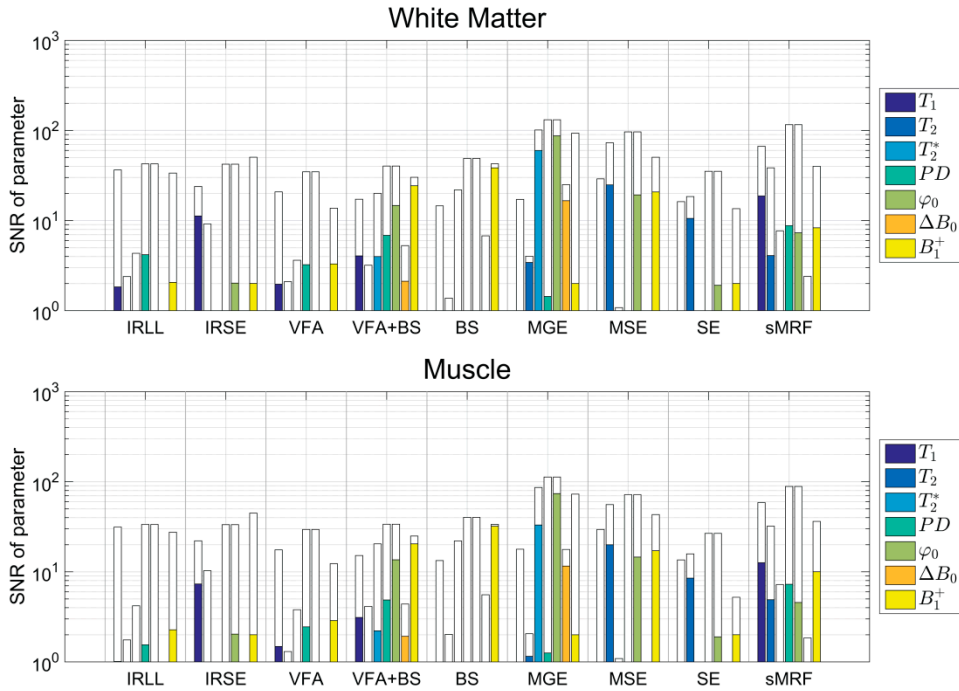


**Figure 3.1.** Results of the simulation study, where the SNR of the parameters was predicted for estimating white matter (top) and muscle (bottom) tissue with each qMRI method in  $T_{ref} = 10$  min acquisition time. Colored bars indicate  $SNR_p^E$ , the SNR when the other parameters are unknown, and white bars indicate  $SNR_p^I$ , the SNR when the other parameters are (assumed) known.

$SNR_p^I$ , the SNR when the other parameters are assumed to be known, and  $SNR_p^E$ , the SNR when the other parameters are unknown. Note that the additional uncertainty yields that  $SNR_p^E \leq SNR_p^I$  for each parameter.

It can be observed that the framework predicts for each qMRI methods a high  $SNR_p^E$  value for the parameters it is conventionally estimates.

For instance, notice the high  $SNR_p^E$  value of  $T_1$  for IRLI and IRSE. Simultaneously, a large difference between  $SNR_p^E$  and  $SNR_p^I$  indicates that precise estimation of the parameter requires knowledge of the other parameters. For example, the VFA method yields a low  $SNR_p^E$  value for  $T_1$  estimation compared to the information  $SNR_p^I$  on this parameter. Further inspection shows that if VFA is combined with the BS method, the  $SNR_p^E$  of  $T_1$  is markedly improved since the uncertainty in  $B_1^+$  is resolved. As the BS method provides information on  $B_1^+$ , but hardly on  $T_1$ , the combination has a slightly lower  $SNR_p^I$  value  $T_1$  (as indicated by a slightly lower white bar), yet yields a substantially higher  $SNR_p^E$ .

Additionally, very low  $SNR_p^E$  for estimating  $T_1$  can be observed for MGE, MSE and SE, and simultaneously a high  $SNR_p^E$  for  $T_2^*$  and  $T_2$  is obtained for respectively MGE and SE/MSE. Also notice that MRF has high  $SNR_p^E$  across all parameters, except  $T_2^*$  and  $\Delta B_0$ .

### Phantom Study

Figure 3.2 shows for different qMRI methods and all 14 ROI's the correlation between the measured and predicted standard deviation for all parameters except  $\varphi_0$ , as it is of little practical interest. Here, we only include the qMRI methods that are rele-

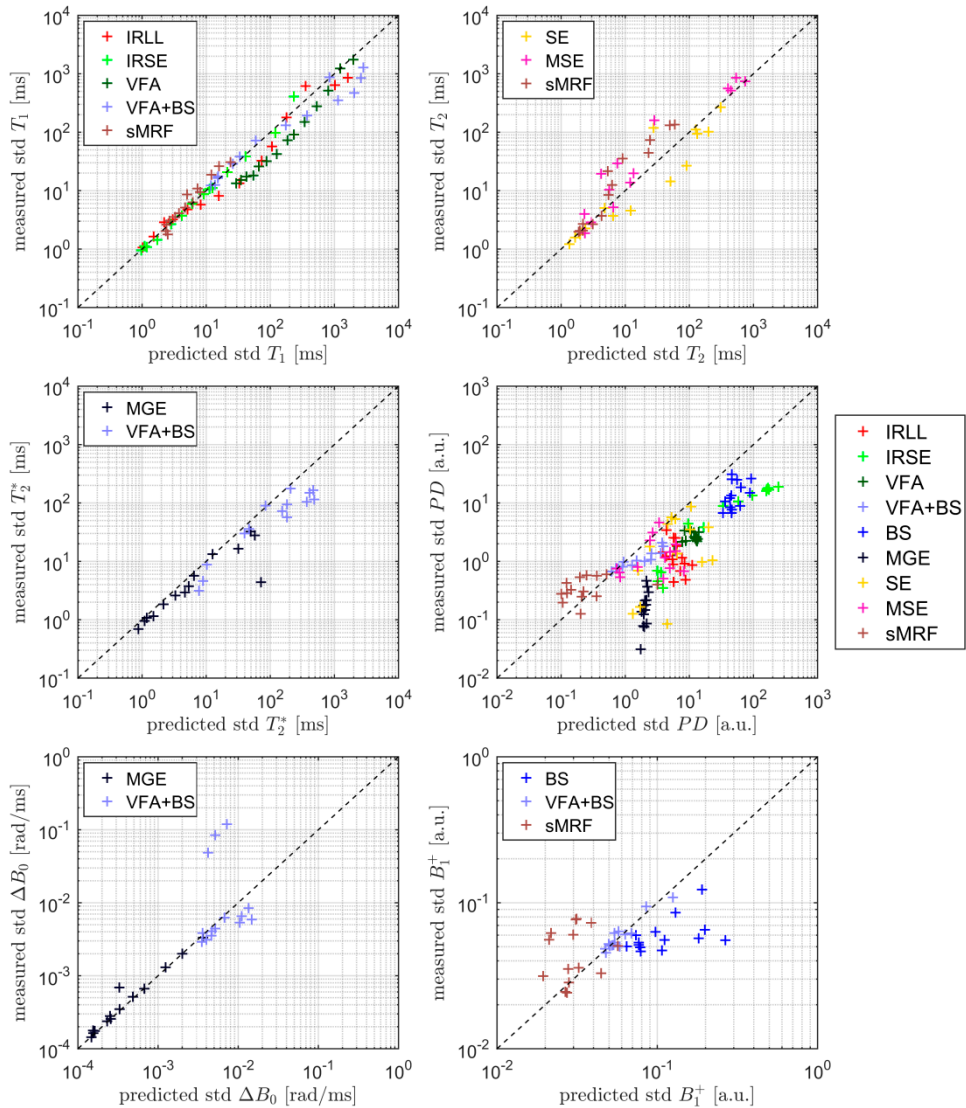


**Figure 3.2.** Results of the phantom study. The scatter plot shows the correlation between predicted and measured standard deviation (std) of the estimated parameters  $T_1$ ,  $T_2$ ,  $T_2^*$ ,  $PD$ ,  $\Delta B_0$ , and  $B_1^+$  in each ROI of the NIST system phantom. For each parameter we only show the relevant qMRI acquisitions, indicated by the legend in each subfigure.

vant for the mapping of a given parameter (see Supporting Figure S3.1 for a complete overview). One may observe that for methods that are known to be precise in estimating certain parameters the observed standard deviations of these parameters closely match the predicted ones. For instance, the predicted and observed standard deviations for estimating  $T_1$  closely match for IRL, IRSE and VFA+BS. This is also the case for the standard deviations of the  $T_2^*$  estimates of MGE and the  $T_2$  estimates of MSE and SE. Exceptions the  $B_1^+$  estimates of MRF and BS, and the  $PD$  estimates of most methods. The qMRI methods that are not practically used for estimating a given parameter typically had a high predicted standard deviation while the measured standard deviation could be much lower (see Supporting Figure S3.1). This was especially the case for  $\Delta B_0$  and  $B_1^+$ . From the  $9(\text{methods}) \times 14(\text{ROIs}) \times 6(\text{parameters}) = 672$  predictions of the standard deviation, there were 94 (12.4%) values below the 95% confidence interval, which predominantly concerned the MRF method that measured lower precision than predicted in 55 cases.

The calibrated  $T_1$  values of the spheres were accurately estimated using the relevant methods (IRLL, IRSE, VFA, VFA+BS, MRF), and this was also the case for the  $T_2$  values (SE, MSE, MRF) (see Supporting Figure S3.2).

## Discussion

In this paper we proposed and validated a new framework for determining the time efficiency of qMRI methods. The precision was predicted through the CRLB and normalized by the acquisition time of a method. The CRLB evaluations were based on Bloch simulations of the MRI signals, which are applicable to any pulse sequence and allow the signal modelling under many relevant assumptions/conditions. Here, we determined the time efficiency of nine qMRI methods for estimating seven parameters ( $T_1, T_2, T_2^*, \Delta B_0, B_1^+, PD, \varphi_0$ ) simultaneously. However, the time efficiency framework is applicable to any combination of qMRI methods and estimated parameter sets that can be accurately modelled through Bloch simulations.

The phantom study showed reasonable agreement between predicted and observed standard deviations over a wide range of precisions, demonstrating that the proposed framework provides meaningful predictions of precision. Especially in the cases with small predicted standard deviation, where it is most relevant, the results closely matched. The exception was MRF which had lower measured precision than predict-

ed. As this method has complicated spin dynamics, we hypothesize that slight differences between what is played out on the scanner and the simulation, as well as limitations of the simulations (see below), increases the difference between the predicted and encountered standard deviations. Future work should further identify the reasons of this discrepancy. For some cases with very low predicted precision, the parameter maps had higher measured precision due to the constrained search domain used for parameter estimation (see Supporting Figure S3.1). However, these cases are not considered relevant for practical application. In particular, when high precision was predicted, the proposed framework showed close correspondence with the measured precision.

As the framework evaluates the time efficiency entirely in simulation, it also facilitates optimizing the time efficiency of a sequence over its settings such as flip angles, inversion times, echo times, etc. A limitation of the proposed time efficiency framework is that it does not explicitly consider the minimum scan time that is required to obtain an image. Hence, there is the implicit assumption that, possibly with parallel imaging and/or advanced image reconstruction methods, the reference scan time can be achieved. Depending on the available scan time, desired field of view, and the resolution, this might not be the case for every qMRI method. Also the effect of artifacts (for instance due to subject motion) is currently not considered by the proposed framework.

A further limitation is that the Bloch simulation used as signal model did not include diffusion, perfusion, flow, etc. Parameters related to these processes were not evaluated either. We did so to assess the ‘pure’ efficiency of the methods under study. However, when performing a more advanced Bloch(-Torrey) simulation that includes parameters on these processes, the time efficiency of sequences with respect to those parameters can also directly be evaluated with the proposed framework.

The list of selected sequences is by no means exhaustive nor are all sequence settings optimal. The aim of the framework is to allow easy evaluation of any sequence. No time-consuming implementation and evaluation on the scanner is needed, only an in-silico pulse sequence simulation. As such we particularly recommend to use the proposed framework when searching for ‘the best’ sequence for estimating quantitative MRI parameters in a tissue of interest.

## Conclusion

This work presented and validated a framework for estimating the precision of quantitative MRI method. The framework enables an objective and in-silico comparison of different methods, and consequently selecting the best method without time-consuming scan experiments.

## Supplementary Materials

### A. Pulse sequences in TOPPE

The TOPPE frameworks consists of a number of modules with five channels (RF amplitude and angle, and the three gradient waveforms), and a text file specifying a timed sequence of these modules with scaling factors of the waveforms and wait time between them.

Each qMRI acquisition was based on a sequence of the following modules:

- *signal readout*, acquiring a single Cartesian line in k-space with balanced gradients;
- *gradient pulse*, providing a maximum of  $40\pi$  rad/cm dephasing in each direction;
- *RF excitation*, providing a maximum of  $90^\circ$  rotation, with 5 mm slice width, 1.1 ms duration, a time-bandwidth product of 3, and balanced gradients;
- *RF inversion*, adiabatic and non-selective inversion using a hyperbolic secant pulse of 10 ms;
- *RF refocusing*, providing  $180^\circ$  rotation with 6 mm slice width, 4 ms duration, a time-bandwidth product of 4;
- *RF off-resonance pulse*, a Fermi pulse of 10 ms, played at  $\pm 4$  kHz off-resonance.

The excitation and refocusing RF pulses are designed using the Shinnar-Le Roux algorithm from John Pauly's RF toolbox. While the above mentioned design of the modules is easy to use and very flexible, the timing typically cannot be as strict as dedicated sequence implementations. The sequence files that we used are provided through [https://bitbucket.org/bigr\\_erasmusmc/time-efficiency](https://bitbucket.org/bigr_erasmusmc/time-efficiency).

## B. Parameter Discretization

**Table S3.1** Parameter discretization in the signal dictionaries of each qMRI method. The knot points are sampled uniformly from the range shown for each parameter in Table 3.2. The number of knot points is chosen to obtain a maximal interpolation error of  $10^{-3}$  along the given dimension with B-spline order 2. Note that the interpolation threshold is often obtained with a small number of knot points, since the solution of the Bloch equations mostly varies smoothly with the underlying parameters [56].

qMRI method	number of knot points				
	$\log(T_1)$	$\log(T_2)$	$\log(T_2')$	$\Delta B_0$	$B_1^+$
IRLL	8	5	3	7	3
IRSE	8	6	3	6	11
VFA	5	4	3	7	7
VFA + BS	5	4	3	16	3
BS	6	6	4	24	4
MGE	6	7	6	221	4
SE	7	7	3	3	11
MSE	8	6	4	3	25
MRF	9	5	4	9	5

### C. Complete Time Efficiency Validation

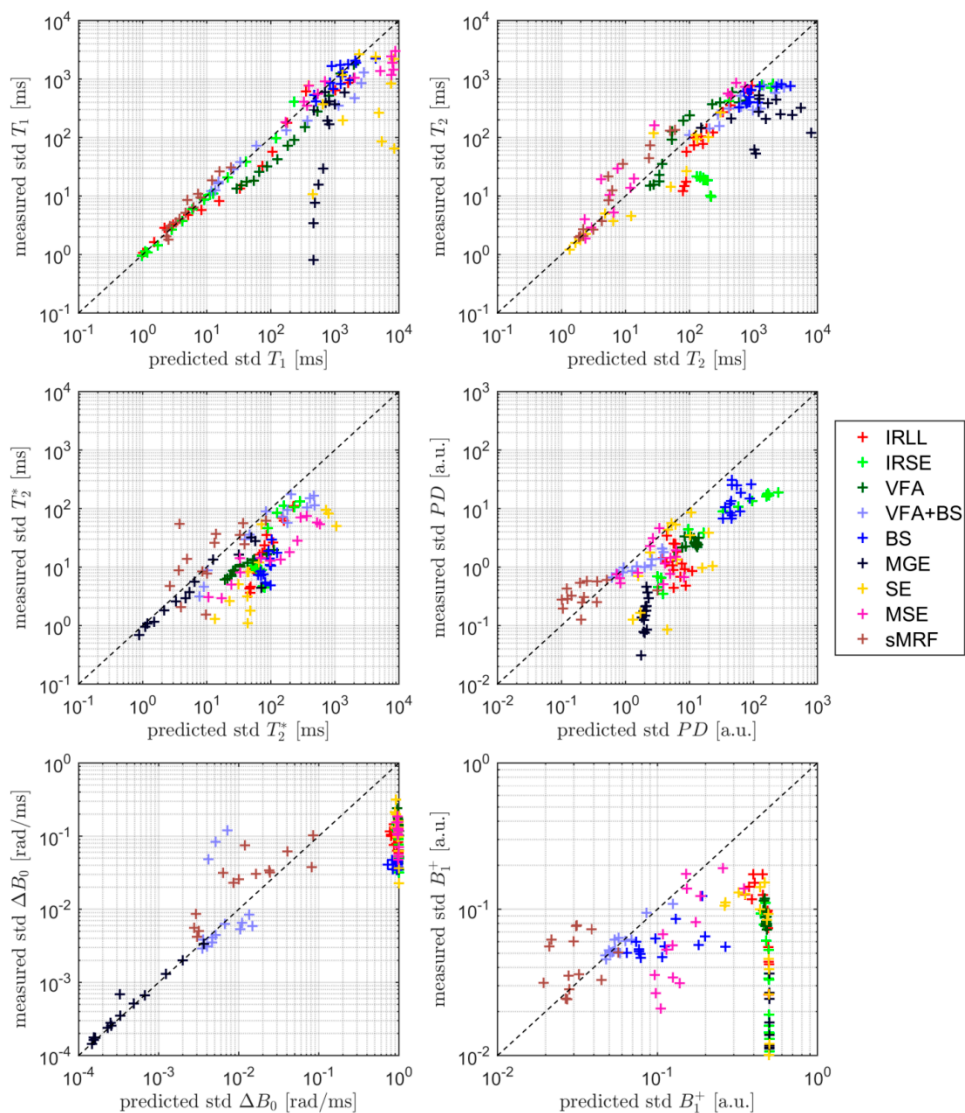


**Figure S3.1.** Results of the phantom study for all combinations of method and parameter. The scatter plot shows the correlation between predicted and measured standard deviation (std) of the estimated parameters  $T_1$ ,  $T_2$ ,  $T_2^*$ ,  $PD$ ,  $\Delta B_0$ , and  $B_1^+$  in each ROI of the NIST system phantom. Note that for some parameter (e.g.  $\Delta B_0$ ,  $B_1^+$ ) with high predicted standard deviation, the measured standard deviation is substantially lower since the parameters are estimated within a restricted domain.

### D. Relaxometry Estimation Accuracy

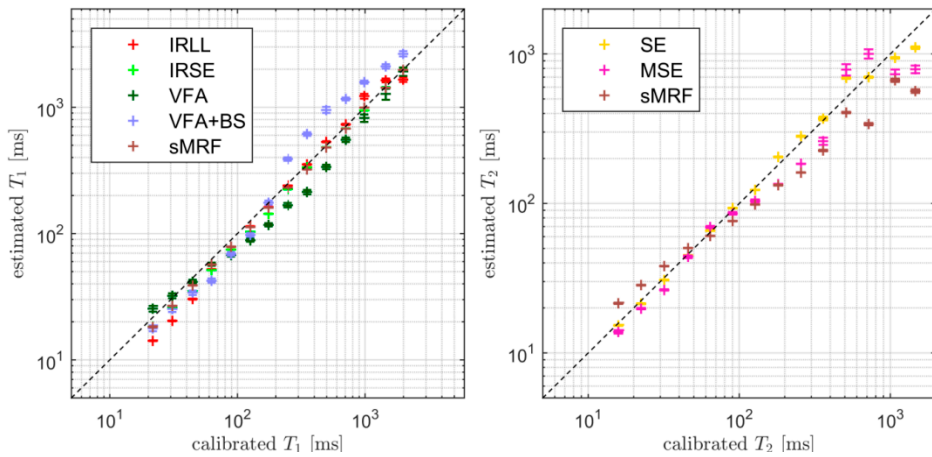


**Figure S3.2.** Scatter plot that compares the mean estimated  $T_1$  and  $T_2$  values of each ROI of the NIST system phantom to their calibrated values for the relevant qMRI methods.



# Protocol Optimization

# Simultaneous Estimation of Multiple Parameters from an Optimized Combination of Quantitative MRI Methods

Willem van Valenberg, Frans M. Vos, Stefan Klein, Lucas J. van Vliet, Dirk H.J. Poot

## Abstract

When multiple physical parameters are of interest, the estimation of each parameter with sufficient precision and accuracy in a short scan time is problematic. Quantitative MRI (qMRI) methods with high accuracy and precision conventionally require long scan times, while shorter methods are susceptible to bias due to complex signal dynamics. We aim to increase the accuracy and precision obtained in a single scan by simultaneously estimating multiple parameters from an optimal combination of (short) qMRI methods.

A scan protocol is defined from a set of 11 qMRI methods by selecting for each method the number of averages and method-specific settings (e.g. flip angles, echo times) that maximize the precisions of the estimated parameters in the available scan time. The precisions are predicted through the Cramér-Rao lower bound (CRLB) from Bloch simulations of the MR signal. We apply a block-wise optimization scheme that alternates between optimizing the number of averages through a genetic algorithm, and optimizing the settings of each methods through a direct gradient-based algorithm. We balance precision and scan time by adjusting a regularization parameter ( $\lambda$ ) in the cost function. Here, we optimize to obtain maximal precision for relaxometry values ( $T_1, T_2, T_2'$ ) while accounting for confounding parameters related to the proton density ( $PD$ ) and magnetic fields ( $\Delta B_0, B_1^+, \varphi_0$ ).

The optimized scan protocols were found to be reproducible and obtained higher precisions for most parameters than dedicated reference methods with the same scan time. The exception was the  $T_2$  estimation through the multiple spin echo method. While validation of the predicted precisions in a scan experiment is still required, the proposed optimization framework is promising for developing scan protocols with a short scan time that can estimate multiple parameters with accuracy and precision.

## Introduction

Quantitative MRI methods measure the physical parameters that determine the MR signal such as the  $T_1$  and  $T_2$  relaxation constants. It is usually assumed that these parameters are more reproducible than the signal in a conventional MR image that depends on the varying static ( $B_0$ ) and transmit ( $B_1^+$ ) magnetic fields. Conventionally, parameter estimation relies on a number of dedicated methods such as the variable flip angle method for  $T_1$  mapping [52], the multiple spin-echo method for  $T_2$  mapping [11], or the Bloch-Siegert shift method for  $B_1^+$  mapping [53].

Clearly, when multiple qMRI parameters are of interest, each parameter may be estimated separately or in some cases sequentially. However, recent work showed that for  $T_1$  and  $T_2$  mapping, the precision of the parameter estimates could be substantially improved by fitting a combined signal model of the two dedicated acquisitions (SPGR and SSFP) instead of performing sequential fits [40]. A further increase in precision was obtained by optimizing the acquisition settings (of SPGR and SSFP) through the Cramér-Rao lower bound, which was also applied for combinations of SPGR and DESS acquisitions [38].

These techniques are appropriate for the simultaneous estimation of parameters based on an a priori defined combination of qMRI methods. However, there is a large variety of methods and consequently the number of possible combinations that can be performed in a fixed scan time is immense. In effect, an exhaustive search over all possible combinations is computationally infeasible, especially when acquisition settings also need to be optimized. Additionally, there are practical difficulties in the construction of combined signal models as often each signal model is derived under special assumptions and may ignore effects that do not confound the parameters of primary interest (e.g. modulation of the estimated proton density,  $PD$ , by  $T_1$  in a  $T_2$  spin-echo experiment, or conversely by  $T_2$  in a  $T_1$  inversion-recovery experiment).

In this paper, we study a theoretical framework for the design of a protocol to estimate an arbitrary combination of quantitative parameters. We hypothesize that this enables development of such a protocol in a generalized way. The framework is demonstrated by optimizing the combination of qMRI methods for the estimation of relaxometry values ( $T_1, T_2, T_2'$ ) while accounting for confounding effects due to the proton density

( $PD$ ), RF transmit amplitude ( $B_1^+$ ) and receive phase ( $\varphi_0$ ), and static field inhomogeneities ( $\Delta B_0$ ).

## Methods

### *Theoretic Precision*

We constructed a scan protocol from a set of  $Q$  quantitative methods for relaxometry, for example: multiple-gradient echo (MGE), inversion-recovery spin echo (IRSE), and MR Fingerprinting (MRF). Each method, indexed by  $q$ , had  $K_q$  acquisitions settings (i.e. applied flip angles and repetition/echo/inversion times) which were combined in a vector  $\boldsymbol{\phi}_q \in \mathbb{R}^{K_q}$ . With these settings, each method acquired  $M_q$  contrast images: the different echoes for MGE, inversion-times for IRSE, or repetitions in MRF. Note that  $M_q$  was not considered one of the acquisitions settings but specific for the method (i.e. MGE with 16 or 32 echoes were considered different methods). Each method was assumed to sample a consistent acquisition matrix, leading to a scan time of  $t_q(\boldsymbol{\phi}_q)$  for a fully-sampled acquisition.

After image reconstruction, each voxel had a signal time course  $\mathbf{m}_q \in \mathbb{C}^{M_q}$  based on  $P$  voxel-dependent parameters  $\boldsymbol{\theta} = [\theta_1, \dots, \theta_P] \in \Theta \subseteq \mathbb{R}^P$ , which described the relaxometry ( $T_1, T_2, T_2'$ ), proton density ( $PD$ ), and the transmit ( $B_1^+$ ) and static ( $\Delta B_0$ ) magnetic field. The signal  $\mathbf{m}_q \in \mathbb{C}^{M_q}$  can be modelled through the method-specific solution of the Bloch equations,  $\mathbf{s}_q(\boldsymbol{\theta}, \boldsymbol{\phi}_q)$ , with a noise contamination  $\boldsymbol{\sigma}_q$ :

$$\mathbf{m}_q = \mathbf{s}_q(\boldsymbol{\theta}, \boldsymbol{\phi}_q) + \boldsymbol{\sigma}_q \in \mathbb{C}^{M_q} \quad (4.1)$$

The noise  $\boldsymbol{\sigma}_q$  was assumed to be uncorrelated between measurements and receiver channels and identically Gaussian distributed with variance  $\sigma_q^2 \in \mathbb{R}$ . In this case, the information a given method obtained on the parameters  $\boldsymbol{\theta}$  could be described by the Fisher information matrix [28]:

$$\mathbf{I}_q(\boldsymbol{\theta}, \boldsymbol{\phi}_q) = \frac{1}{\sigma_q^2} \left( \frac{\partial \mathbf{s}_q(\boldsymbol{\theta}, \boldsymbol{\phi}_q)}{\partial \boldsymbol{\theta}} \right)^H \left( \frac{\partial \mathbf{s}_q(\boldsymbol{\theta}, \boldsymbol{\phi}_q)}{\partial \boldsymbol{\theta}} \right) \in \mathbb{R}^{P \times P} \quad (4.2)$$

The matrix  $\mathbf{I}_q(\boldsymbol{\theta}, \boldsymbol{\phi}_q)^{-1}$  is a lower bound on the covariance matrix of unbiased estimates of  $\boldsymbol{\theta}$  from the measured signal  $\mathbf{m}_q$  [28]. Therefore, the diagonal of

$I_q(\boldsymbol{\theta}, \boldsymbol{\phi}_q)^{-1}$  contains the minimal variance (i.e. maximal precision) with which  $\boldsymbol{\theta}$  can be accurately estimated.

To design a scan protocol, we aimed to combine the information from the separate qMRI methods in an optimal manner for a set of  $N_\theta$  parameter values of interest  $\{\boldsymbol{\theta}_i\}_{1 \leq i \leq N_\theta}$ . For each method we select the number of repeats  $n_q$ , and assume that the noise in each image has equal variance  $\sigma_q^2 = \sigma^2$  for  $1 \leq q \leq Q$ . In this case, the total information obtained through the protocol equals:

$$\mathbf{I}(\boldsymbol{\theta}; \mathbf{n}, \boldsymbol{\phi}) = \mathbf{I}_{prior} + \sum_{q=1}^Q n_q \mathbf{I}_q(\boldsymbol{\theta}, \boldsymbol{\phi}_q) \in \mathbb{R}^{P \times P} \quad (4.3)$$

Here,  $\mathbf{I}_{prior}$  enabled the inclusion of prior information on the parameters in  $\boldsymbol{\theta}$ ,  $H$  indicates the Hermitian conjugate, and  $\boldsymbol{\phi} = \{\boldsymbol{\phi}_q\}_{1 \leq q \leq Q}$ . The prior information prevents the parameter estimation to obtain unrealistic parameter combinations. When averaging over  $n_q$  repeats, the Gaussian noise in the images scales as  $\sigma^2/n_q$ . While this is theoretically only true for discrete  $n_q$ , we allowed for  $n_q$  to be fractional in the optimization to represent undersampling of images and consequently enable more practical scan times. The protocol defined by  $\mathbf{n}$  and  $\boldsymbol{\phi}$  was expected to estimate the parameters  $\boldsymbol{\theta}$  with a minimal variance of  $\mathbf{I}(\boldsymbol{\theta}; \mathbf{n}, \boldsymbol{\phi})^{-1}$ .

The minimal scan time of the protocol described by  $\mathbf{n}$  and  $\boldsymbol{\phi}$ , not including preparation of each method, is given by:

$$T_{scan}(\mathbf{n}, \boldsymbol{\phi}) := \sum_{q=1}^Q n_q t_q(\boldsymbol{\phi}_q) \quad (4.4)$$

Obviously, a protocol is desired that obtains the highest precision (i.e. lowest variance) of each parameter estimate with the smallest scan time.

### **Protocol Optimization**

To determine the number of repeats  $\mathbf{n}$  and settings  $\boldsymbol{\phi}$  for each method that gives the protocol the highest precision in the shortest scan time for the  $N_\theta$  parameter values of interest,  $\{\boldsymbol{\theta}_i\}_{1 \leq i \leq N_\theta}$ , we defined the following cost function:

$$C(\mathbf{n}, \boldsymbol{\phi}, \lambda) = \left( \sum_{i=1}^{N_\theta} \|\mathbf{W}_i^T \text{diag}(\mathbf{I}(\boldsymbol{\theta}_i; \mathbf{n}, \boldsymbol{\phi})^{-1})\|_2^2 \right)^{\frac{1}{2}} + \lambda T_{scan}(\mathbf{n}, \boldsymbol{\phi}) \quad (4.5)$$

Here,  $\mathbf{W}_i = \text{diag}(\mathbf{w}_i) \in \mathbb{R}^{P \times P}$  weights the importance of the predicted variances of each parameter estimate on the diagonal of  $\mathbf{I}(\boldsymbol{\theta}_i; \mathbf{n}, \boldsymbol{\phi})^{-1}$ . The value of  $\lambda \in \mathbb{R}_{>0}$  is user-specified and determines the relative weight of the scan time  $T_{scan}(\mathbf{n}, \boldsymbol{\phi})$  on the cost. Note that we emphasize the maximization of the minimal precision by taking the 2-norm over the expected variances of each parameter combination of interest.

The goal is to find for a given  $\lambda$  the optimal number of repeats  $\mathbf{n}_{opt}$  and settings  $\boldsymbol{\phi}_{opt}$  of each method:

$$[\mathbf{n}_{opt}, \boldsymbol{\phi}_{opt}] = \arg \min_{\mathbf{n}, \boldsymbol{\phi}} C(\mathbf{n}, \boldsymbol{\phi}, \lambda) \quad (4.6)$$

Observe that small  $\lambda$  in Eq. 4.5 will give high precision protocols with long scan time, and reversely high  $\lambda$  give short scan time and low precision.

Unfortunately, the optimization of Eq. 4.6 is not trivial since evaluating the derivative with respect to  $\boldsymbol{\phi}$  has a high computational complexity due to the required Bloch simulations (details below). Therefore, we applied a block-wise coordinate descent method that alternately solved:

1.  $\arg \min_{\mathbf{n}} C(\mathbf{n}, \boldsymbol{\phi}, \lambda)$  with  $\boldsymbol{\phi}$  fixed
- and subsequently for each  $q$  :
2.  $\arg \min_{n_q, \boldsymbol{\phi}_q} C(\boldsymbol{\phi}, \mathbf{b}, \mathbf{w})$  with  $n_j, \boldsymbol{\phi}_j$  fixed for  $j \neq q$
- (4.7)

For the first step, we applied the genetic algorithm of MATLAB's global optimization toolbox with a population size of 1500, and convergence is achieved if the cost reduction was below  $10^{-5}$  in 500 steps. Here, the computational complex  $\mathbf{I}_q(\boldsymbol{\theta}, \boldsymbol{\phi}_q)$  has to be evaluated only once for each  $q$  since it does not depend on  $\mathbf{n}$ . In the second step, we used the gradient descent method that was stopped when the relative cost reduction was below  $10^{-3}$  in subsequent steps or after 500 iterations. Here, each method is optimized subsequently and requires only the re-evaluation of  $\mathbf{I}_q(\boldsymbol{\theta}, \boldsymbol{\phi}_q)$  for the cur-

rent  $q$ . The full optimization procedure terminated if the relative change in cost was below  $10^{-3}$  or after 100 iterations.

### Signal Simulation

Finding the optimal protocol in Eq. 4.6 requires determining the information  $I_q(\boldsymbol{\theta}, \boldsymbol{\phi}_q)$  in Eq. 4.7 through simulation of the signal  $\mathbf{s}_q(\boldsymbol{\theta}, \boldsymbol{\phi}_q)$  of each method. The signal model was constructed using an event-based Bloch simulator that combined the waveforms and signal readout times of each qMRI method into a single ordered sequence. The computational complexity of the simulation was reduced by modelling the radiofrequency pulses and gradient waveforms as instantaneous pulses and ignoring the k-space trajectory. Thus, the signal was simulated as though there was but a single voxel, which enabled to study the ‘pure’ estimation properties of the qMRI methods and to exclude the influence of differing k-space samplings. Each simulation was initialized by repeating the sequence for an acquisition time of at least 5 seconds. The derivative in Eq. 4.2 is numerically approximated with a central difference method with a step size of 1% of the parameter value.

In this work, each method estimates seven voxel-dependent parameters: proton density ( $PD$ ), longitudinal relaxation time ( $T_1$ ), transversal relaxation time ( $T_2$ ), apparent transversal relaxation time ( $T_2^*$ ), the off-resonance ( $\Delta B_0$ ) field, RF transmit ( $B_1^+$ ) field, and transmit-receive phase ( $\varphi_0$ ). The  $T_2^*$  relaxation was simulated using 5000 spins with off-resonance frequencies that were Cauchy distributed around  $\gamma\Delta B_0$  with scale  $T_2'^{-1} = T_2^{*-1} - T_2^{-1}$ .

## Experiments

The protocol optimization framework was applied to the simultaneous estimation of  $P = 7$  parameters  $\boldsymbol{\theta} = (T_1, T_2, T_2', PD, \varphi_0, \Delta B_0, B_1^+)$ . Here, the relaxometry parameters ( $T_1, T_2, T_2^*$ ) are of main interest, and the other parameters are included to increase the accuracy of the relaxometry parameters. We investigated 11 different quantitative methods for inclusion in the protocol: spoiled gradient-recalled echoes (SPGR), inversion-recovery Look-Locker (IRLL), inversion-recovery spin echoes (IRSE), spin echoes (SE), multiple spin echoes (MSE), steady state free precession (SSFP), double echo steady state (DESS), multiple gradient echoes (MGE), Bloch-Siegert shift (BS), actual flip-angle imaging (AFI), and magnetic resonance fingerprint-

ing (MRF). Table 4.1 lists for each of these methods their initial settings, the bounds on the settings, and a literature reference.

The precision of the relaxometry parameters was quantified by determining for each parameter combination  $\{\boldsymbol{\theta}_i\}_{1 \leq i \leq N_\theta}$  the expected coefficient-of-variation (CoV):

$$\text{CoV}_p(\boldsymbol{\theta}_i; \mathbf{n}, \boldsymbol{\phi}) := \frac{\sqrt{(I(\boldsymbol{\theta}_i; \mathbf{n}, \boldsymbol{\phi})^{-1})_{p,p}}}{\theta_{i,p}}, \quad \text{for } T_1, T_2, T_2' \quad (4.8)$$

The minimization of  $C(\mathbf{n}, \boldsymbol{\phi}, \lambda)$  was done using  $w_{i,p} = \theta_{i,p}$  for  $T_1, T_2, T_2'$  (the parameters of interest) and  $w_{i,p} = 0$  for  $PD, \varphi_0, \Delta B_0, B_1^+$  (considered of indirect interest). The optimization was performed for tissue parameters corresponding to white matter ( $T_1/T_2 = 1084/69$  ms) and grey matter ( $T_1/T_2 = 1412/50$  ms). These  $T_1$  and  $T_2$  values were taken from [57], while for the other parameters we chose:  $T_2' = 100$  ms,  $PD = 1$ ,  $\varphi_0 = 0$  rad. The protocol optimization was applied to the two tissues for 10 combinations of  $B_1^+$  and  $\Delta B_0$ , sampled from respectively  $[0.85, 1.15]$  and  $[-100, 100]$  Hz, using a Halton search. This yielded 20 test parameter settings  $\boldsymbol{\theta}_i$  in Eq. 4.5 in total. Furthermore, we investigated the effect on scan time and the precisions of varying  $\lambda$ , by optimizing with ten values of  $\lambda$  logarithmically spaced between  $10^{-4}$  and  $10^{-1}$ .

The genetic algorithm in the optimization includes a random initialization of the weights  $\mathbf{n}$ . We restarted the optimization five times to investigate the reproducibility of the resulting protocol costs, precisions, durations, and compositions. Additionally, the theoretic precisions of the optimized protocols were compared to theoretic precisions of standard qMRI methods, where both were determined through Eq. 4.8.

**Table 4.1.** Methods and settings included in the protocol optimization, with a literature reference for each method. Settings are specified by name, unit, range of potential values, and their initial value(s) of each of the number of versions included of a method (shown in parentheses below the method name). The settings are: flip angle ( $FA$ ), repetition/inversion/echo/delay times ( $T_R/T_I/T_E/T_D$ ), number of measurements ( $M_q$ ), echo spacing ( $ESP$ ), Bloch-Siegert shift ( $\varphi_{BS}$ ), and RF phase shift between subsequent pulses ( $\psi_{RF}$ ).

method (#)	settings ( $\phi_q$ )				literature reference
	name	unit	range	initial value(s)	
SPGR (3)	$FA$ $T_R$	$^\circ$ ms	[0,60] [10, $\infty$ )	{9, 15, 30} {10, 10, 10}	[52]
IRLL (2)	$M_q$ $T_I$ $FA$ $ESP$ $T_D$	– ms $^\circ$ ms ms	– [3.8, $\infty$ ) [0,60] [10.1, $\infty$ ) [13, $\infty$ )	{16, 32} {10, 10} {15, 15} {15, 15} {100, 100}	[50]
IRSE (3)	$T_I$ $T_E$ $T_D$	ms ms ms	[3.8, $\infty$ ) [13, $\infty$ ) [16, $\infty$ )	{30, 530, 1030} {15, 15, 15} {1600, 1600, 1600}	[51]
SE (4)	$T_E$ $T_D$	ms ms	[13, $\infty$ ) [6, $\infty$ )	{20, 40, 80, 160} {50, 50, 50, 50}	[55]
MSE (2)	$M_q$ $T_D$ $ESP$	– ms ms	– [5.3, $\infty$ ) [14.2, $\infty$ )	{8, 16} {50, 50} {15, 15}	[11]
MGE (3)	$M_q$ $FA$ $T_D$ $ESP$	– $^\circ$ ms ms	– [0, 90] [6, $\infty$ ) [5, $\infty$ )	{8, 16, 32} {20, 20, 20} {50, 50, 50} {5, 5, 5}	[54]
BS (2)	$FA$ $\varphi_{BS}$ $T_D$	$^\circ$ $^\circ$ ms	[0, 90] [22.2, –22.2] [6.3, $\infty$ )	{20, 20} {22.2, –22.2} {10, 10}	[53]
AFI (1)	$FA$ $T_{R,1}$ $T_{R,2}$	$^\circ$ ms ms	[0, 90] [10, $\infty$ ) [10, $\infty$ )	{60} {20} {100}	[8]
SSFP (3)	$FA$ $T_R$ $\psi_{RF}$	$^\circ$ ms $^\circ$	[0, 80] [8.1, $\infty$ ) [0, 360]	{20, 60, 80} {8.1, 8.1, 8.1} {180, 180, 180}	[4]
DESS (1)	$FA$ $T_R$ $\psi_{RF}$	$^\circ$ ms $^\circ$	[0, 80] [15.3, $\infty$ ) [0, 360]	{10} {28} {180}	[58]
MRF (1)	$T_D$	ms	[13, $\infty$ )	{20}	[14]

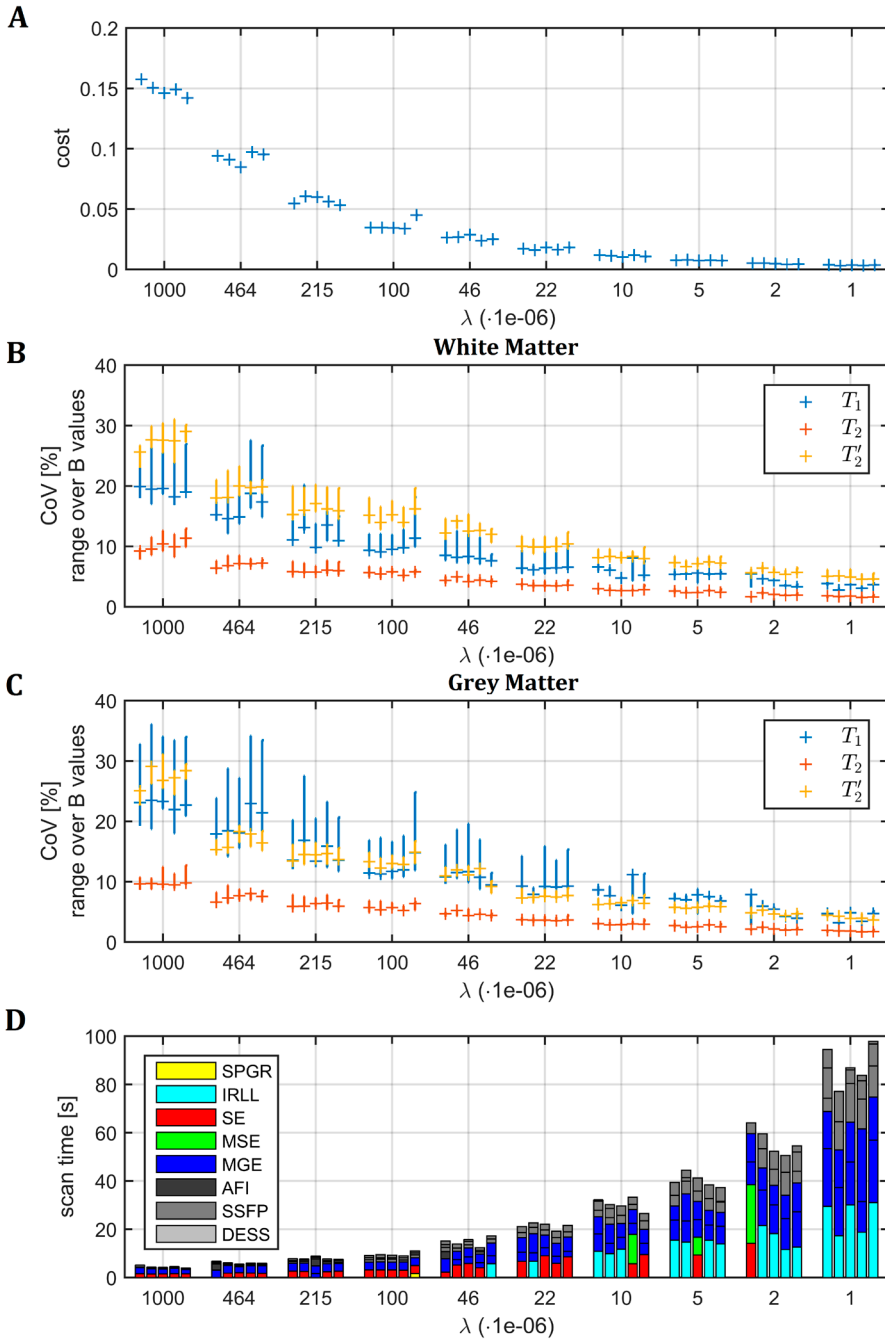
## Results

Figure 4.1 (A) shows the cost of the protocol (Eq. 4.5) that resulted from the optimization procedure as a function of the applied regularization weight ( $\lambda$ ). Each group of five results reflect the outcomes after restarting the optimization five times while applying the same value for  $\lambda$ . Observe that the cost at each value for  $\lambda$  shows little variation between repeats. Furthermore, the cost decreases with decreasing  $\lambda$ .

Figure 4.1 (B,C) depict the theoretic precision (Eq. 4.8) of the parameters of interest ( $T_1, T_2, T_2'$ ) as a function of  $\lambda$  for white and grey matter respectively. The vertical bars represent the range of  $\text{CoV}_p$  values for the optimized protocol across 10 sampled  $B_1^+$  and  $\Delta B_0$  combinations. Furthermore, each horizontal line corresponds to the setting for which  $B_1^+ = 1$ , and  $\Delta B_0 = 0$ . Both graphs confirm that indeed  $\text{CoV}_p$  is improving with decreasing  $\lambda$ .

Finally, Figure 4.1 (D) shows the scan time of the optimized protocols as a function of  $\lambda$ . Moreover, the colors in the bars reflect the composition of the resulting protocols. It can be observed that there is again little variation both in composition and scan time across the repeated optimizations. The graph demonstrates that indeed the scan time increases with decreasing  $\lambda$ .

Figure 4.2 shows the theoretic precision of the parameters of interest as a function of the scan time while applying different protocols, for white and grey matter. Markers indicate precisions of the optimized protocols with  $B_1^+ = 1$ , and  $\Delta B_0 = 0$ , while error bars represent the range in values across repeats. Lines represent the precisions (Eq. 4.8) for reference methods when simultaneously estimating each parameter ( $T_1, T_2, T_2^*, PD, \varphi_0, \Delta B_0, B_1^+$ ). Observe that the scan durations of both the optimized and reference protocols varied through differing numbers of signal averages. The line styles reflect different levels of undersampling: acceleration factors of more than two are depicted with dashed lines. As expected, all curves follow a  $1/\sqrt{t}$  profile. Furthermore, it can be observed that in general the precisions of the optimized protocol are improved (reflected by lower CoV values) compared to the standard qMRI methods. Only the dedicated MSE method gives slightly better outcome for quantification of  $T_2$ , while requiring high acceleration factors for scan times within 1 minute. Furthermore, the optimized protocol additionally has good precision for  $T_1$  and  $T_2'$ .



**Figure 4.1.** Protocol optimization outcomes for varying regularization weight ( $\lambda$ ); each group of five results represents the outcomes after restarting the procedure five times at the same value of  $\lambda$ : (A) protocol cost after optimization; (B,C) ranges of theoretic precision, i.e. coefficient of variation (CoV) of the relaxometry parameters  $T_1, T_2, T_2'$  across different parameter settings  $\theta_i$  for white matter and grey matter; (D) scan times and composition of protocols.

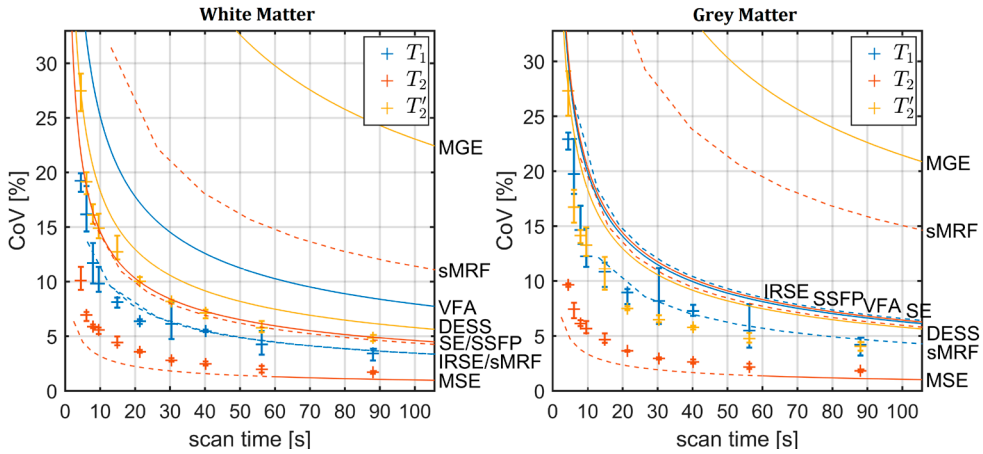


**Figure 4.2.** Theoretic precision (Eq. 4.8) of parameters of interest as a function of the scan time applying different protocols, for white and grey matter. Markers indicate the precision for optimized protocols with  $B_1^+ = 1$  and  $\Delta B_0 = 0$ , while the bars reflect the range variation over repeats. Lines represent the precision obtained through reference methods for different levels of undersampling: acceleration factors of more than two are depicted by dashed lines.

## Discussion

This chapter presented a framework for the design of quantitative protocols that simultaneously estimate multiple parameters ( $T_1, T_2, T_2', PD, \varphi_0, \Delta B_0, B_1^+$ ) in a short scan time. The methods and their settings were optimized to obtain the highest expected precision in the available scan time through an unbiased estimator. The framework applied a block-wise optimization method where the number of averages of each method was determined through a genetic algorithm and the settings through direct gradient-based optimization. The optimized protocols had a cost and composition of methods that were reasonably consistent over multiple restarts of the genetic algorithm. Furthermore, protocols of increasing scan time, and consequently precision, were found by varying the regularization parameter ( $\lambda$ ). With strong regularization, the framework was guided to short qMRI methods, while weaker regularization enabled the inclusion of longer methods (e.g. IRLL). Surprisingly, the optimized protocol had higher precisions for most parameters than their dedicated reference methods with the same scan time, with the exception of  $T_2$  estimation through MSE. While the precisions of the reference methods can be improved by optimizing their settings, the optimized protocol seem to achieve comparable precision while estimating multiple parameters simultaneously.

The precisions, as determined through the Cramér-Rao lower bound, are predictive of the maximal precisions that can be found in practice with an unbiased estimator. However, these predictions have not been validated for the optimized protocols. Multiple reference methods have had their CRLB-predicted precisions validated (see Chapter 3) for fully-sampled acquisitions. In this work, we specifically allowed for undersampling of the data in the optimization framework under the assumption of predictive noise behavior. Finding k-space trajectories and reconstruction methods to approximate this desired behavior is not trivial, and an important extension of this work.

The optimization framework can be extended through the inclusion of more qMRI methods and estimated parameters. Signal simulation is done through the Bloch equations which models most MR pulse sequences and can include additional physical effects (e.g. motion, diffusion, magnetization transfer). The modelling of additional effects and methods might require smart simulation strategies. However, as the computational complexity of the Fisher information (Eq. 4.3) practically increases linearly with the number of estimated parameters and included qMRI methods that is not expected to be a limiting factor. This work was focused on the estimation of relaxation times ( $T_1, T_2, T_2'$ ) since the selection of an optimal protocol is difficult due to the wide range of possible methods for their estimation.

The simultaneous estimation of parameters ( $T_1, T_2, T_2', PD, \varphi_0, \Delta B_0, B_1^+$ ) through an optimized protocol increased the expected precisions compared to a combination of dedicated methods for each parameter. Consequently, this enables the accurate and precise estimation of multiple parameters in a short scan time.



# Conclusions and Discussion

Quantitative MRI (qMRI) methods measure the physical parameters that determine the MR signal with the aim of improving the reproducibility and interpretability of MRI data. Although qMRI methods have been used for many years, widespread application to the clinic has been limited. This is partly due to the long scan times that traditional methods require to obtain a parameter map with acceptable accuracy and precision. Faster quantitative methods can estimate parameters inaccurately by ignoring confounding physical effects in order to simplify the parameter estimation. This thesis introduced novel methods aiming to improve the efficiency of qMRI methods by simultaneously estimating more parameters from a single scan, with higher accuracy and precision.

### ***A computationally efficient method for multi-parameter mapping***

MR Fingerprinting methods estimate multiple physical parameters simultaneously by matching a measured signal to a so-called dictionary: the simulated signals for a fine grid of parameter combinations. However, accurate parameter estimation requires discretizing the parameters with a high resolution, which requires large computational and memory costs for dictionary generation, storage, and matching.

In **Chapter 2** of this thesis, a technique was introduced for enhancing the efficiency of the parameter mapping. The method was based on fitting a measured signal to a sparse signal dictionary that was interpolated using B-splines. This is especially beneficial when estimating multiple ( $>3$ ) parameters simultaneously, which is computationally infeasible for alternative methods such as dictionary matching or a direct fit of the Bloch equations. As such, it facilitates that additional parameters can be included in the fitting to account for confounding factors such as magnetic field inhomogeneities. This technique was applied to a wide range of quantitative methods in Chapters 2 and 3, such as inversion-recovery (quantifying  $T_1$ ), multiple gradient-echo ( $T_2^*$ ), and Bloch-Siegert ( $B_1^+$ ). Application to this large diversity of methods illustrates the versatility of the presented technique, making it a useful tool for future development of multi-parametric quantitative methods. In recent years, machine learning techniques have become an interesting alternative for the parameter estimation of qMRI methods. Machine learning is promising for estimating parameters with a short scan time, but the underlying factors that determine their outcome are still poorly understood. Essentially, by using a dictionary generated using a general physical model, the method for multi-parametric mapping presented in Chapter 2 can bridge the gap between the

computationally complex model-based estimation of parameters to the efficient data-driven methods based on machine learning.

### ***A time efficiency measure for the comparison of qMRI methods***

The desire for more accurate and reproducible parameter estimation has led to many different measurement methods for each parameter of interest. These methods differ in accuracy (i.e. bias), precision (estimation variance), acquisition time, and features like motion sensitivity, gating capabilities and/or fat suppression. This makes determining the best method for parameter estimation problematic. In any case a measure for the precision of a qMRI method must account for differences in scan time, since every method becomes more precise by averaging over repeated measurements at the expense of increased scan time.

In **Chapter 3**, we proposed a selection criterion, called time efficiency, that reflects the precision that can be achieved in the available scan time. The time efficiency measure is based the Cramér-Rao lower bound, which describes the minimal variance of an unbiased parameters estimate. We normalize the Cramér-Rao lower bound by the duration of the scan to obtain the time efficiency measure that is invariant to the number of averages. Through time efficiency, selection of the best method as well as its settings can be performed in-silico, which avoids costly evaluations on the scanner. The predicted precisions were shown to be representative for a range of qMRI methods and estimated parameters. Practically, the choice of a method is often not solely based on precision, accuracy and scan time, but also on for instance the specific absorption rate (SAR) and system limitations. However, in every experiment there is likely some choice in the applied quantitative method and settings for which the proposed time efficiency measure provides a solution.

### ***Simultaneous estimation of multiple parameters by an optimal combination of qMRI methods***

Conventionally, each parameter has dedicated methods for its measurement. When multiple parameters are of interest, each parameter may be estimated separately or in some cases sequentially from each qMRI method. However, the precision of parameter estimates may be improved by fitting a combined signal model of the dedicated acquisitions instead of performing sequential fits.

**Chapter 4** proposed a framework for the selection of a combination of quantitative methods as well as their settings to obtain maximal precision for a certain set of quan-

titative parameters. It was shown that an optimized combination can estimate multiple parameters with higher precision than most reference methods dedicated for a single parameter. Recent years saw the introduction of a number of methods that aimed to estimate multiple parameters in a short scan time (e.g. MRF, DESPOT, MAGIC). These methods can easily be included in our optimization framework, as shown for the MRF method, and can possibly be improved regarding their settings.

Together, the three contributions of this thesis enabled estimating multiple parameters with high accuracy and precision in a short scan time. While in the work presented not all relevant physics effects are included (e.g. ignoring motion, flow, perfusion), including such effects only requires extending the Bloch simulations underlying the predicted signals. Such extensions are actively researched as well, but was not the topic of the current thesis.

## Outlook

### *Methodology*

This thesis applied the Bloch equations to model the MR signal as a function of several physical parameters. The signal model was used for estimation of parameters (Chapter 2), for determination of time efficiency (Chapters 3), and for optimization of combinations of qMRI techniques (Chapter 4). The simulations modeled the relaxometry ( $T_1, T_2, T_2^*$ ), proton density ( $PD$ ), and magnetic fields ( $\Delta B_0, B_1^+, \varphi_0$ ). However, several effects were ignored that could also be modelled through the Bloch equations such as magnetization transfer, diffusion, and flow. The inclusion in the model of parameters that describe these effects could enable their estimation through the method proposed in Chapter 2. Obtaining high precision estimates will become more challenging when further increasing the number of parameters, but the time efficiency measure proposed in Chapter 3 is a good design tool for this.

Parameter estimation in this thesis was done in a voxel-wise fashion, but some advantages might be gained by taking more data into account (e.g. a neighborhood of voxels). Additionally, instead of parameter estimation from the reconstructed images, the fitting might be done on the k-space data. This could provide a mechanism to better cope with undersampled k-space data and facilitate reduction of scan time.

### ***Applications***

The methodology of quantitative MR methods has advanced rapidly in recent years, and interest is moving to clinical applications. Here, we discuss some applications for quantitative protocols that estimate multiple parameters in a short scan time. Since conventional MR images are a projection of the underlying physical parameters, most of the clinically used non-quantitative images could be replaced by quantitative parameter maps. However, radiologists are far more experienced with interpreting conventional images. Indeed, parameter maps look different regarding contrast and noise (derived from fitting processes). Synthetic MRI applies the obtained parameter maps to simulate MR images with different contrasts, but such images are still somewhat different than clinical images due to partial volume effects and the mentioned reduction of noise. Still, it might be worthwhile to study the potential of qMRI methods for diagnosis, as such images should be more reproducible on different MRI systems.

Clearly, this advantage of improved reproducibility should be further studied in-depth, for instance by comparison of parameter maps over time, between subjects, and between different scanners. Since the obtained parameters have a physical meaning, the values could be more easily interpreted in relation to pathological processes, just like temperature or blood pressure. This can potentially allow for early detection of subtle tissue changes, for instance related to Alzheimer's disease. Finally, while small studies have been performed to determine typical  $T_1$ ,  $T_2$ , and  $T_2^*$  values in tissues, the application of such quantitative parameters in the clinic requires knowing their value and variability in a much wider population, e.g. to know how they vary across gender, age, and with specific diseases. Now that quantitative methods have matured facilitating improved accuracy and precision with shorter scan times, they could be applied in population studies in order to make the next step towards regular clinical use. The methods proposed in this thesis could add to these developments.



## Reference List

- [1] M. A. Ikram, A. van der Lugt, W. J. Niessen, P. J. Koudstaal, G. P. Krestin, A. Hofman, D. Bos, and M. W. Vernooij, “The Rotterdam Scan Study: design update 2016 and main findings,” *Eur J Epidemiol*, vol. 30, no. 12, pp. 1299–1315, Dec. 2015.
- [2] H. L. M. Cheng, N. Stikov, N. R. Ghugre, and G. A. Wright, “Practical medical applications of quantitative MR relaxometry,” *J. Magn. Reson. Imaging*, vol. 36, no. 4, pp. 805–824, Oct. 2012.
- [3] S. C. L. Deoni, “Quantitative Relaxometry of the Brain,” *Top Magn Reson Imaging*, vol. 21, no. 2, pp. 101–113, Apr. 2010.
- [4] S. C. L. Deoni, B. K. Rutt, and T. M. Peters, “Rapid combined T1 and T2 mapping using gradient recalled acquisition in the steady state,” *Magn. Reson. Med.*, vol. 49, no. 3, pp. 515–526, Mar. 2003.
- [5] J. B. M. Warntjes, O. Dahlqvist, and P. Lundberg, “Novel method for rapid, simultaneous T1, T2\*, and proton density quantification,” *Magn Reson Med*, vol. 57, no. 3, pp. 528–537, Mar. 2007.
- [6] D. Ma, V. Gulani, N. Seiberlich, K. Liu, J. L. Sunshine, J. L. Duerk, and M. A. Griswold, “Magnetic resonance fingerprinting,” *Nature*, vol. 495, no. 7440, pp. 187–192, Mar. 2013.
- [7] E. M. Haacke, R. W. Brown, M. R. Thompson, and R. Venkatesan, *Magnetic resonance imaging: physical principles and sequence design*, vol. 82. Wiley-Liss New York, 1999.
- [8] W. van Valenberg, “Radiofrequency pulse design through optimal control and model order reduction of the Bloch equation,” 23-Jul-2015. [Online]. Available: <http://dspace.library.uu.nl/handle/1874/316003>. [Accessed: 11-Jul-2019].
- [9] J. K. Barral, E. Gudmundson, N. Stikov, M. Etezadi-Amoli, P. Stoica, and D. G. Nishimura, “A robust methodology for in vivo T1 mapping,” *Magn. Reson. Med.*, vol. 64, no. 4, pp. 1057–1067, Oct. 2010.
- [10] J. D. Trzasko, P. M. Mostardi, S. J. Riederer, and A. Manduca, “Estimating T1 from multichannel variable flip angle SPGR sequences,” *Magn. Reson. Med.*, vol. 69, no. 6, pp. 1787–1794, Jun. 2013.
- [11] N. Ben-Eliezer, D. K. Sodickson, and K. T. Block, “Rapid and accurate T2 mapping from multi-spin-echo data using Bloch-simulation-based reconstruction,” *Magn. Reson. Med.*, vol. 73, no. 2, pp. 809–817, Feb. 2015.
- [12] D. Hernando, J. P. Haldar, B. P. Sutton, J. Ma, P. Kellman, and Z.-P. Liang, “Joint estimation of water/fat images and field inhomogeneity map,” *Magn. Reson. Med.*, vol. 59, no. 3, pp. 571–580, Mar. 2008.

- [13] D. Hernando, P. Kellman, J. P. Haldar, and Z.-P. Liang, "Robust water/fat separation in the presence of large field inhomogeneities using a graph cut algorithm," *Magn. Reson. Med.*, vol. 63, no. 1, pp. 79–90, Jan. 2010.
- [14] Y. Jiang, D. Ma, N. Seiberlich, V. Gulani, and M. A. Griswold, "MR fingerprinting using fast imaging with steady state precession (FISP) with spiral readout," *Magn. Reson. Med.*, vol. 74, no. 6, pp. 1621–1631, Dec. 2015.
- [15] Y. Jiang, D. Ma, K. Wright, N. Seiberlich, V. Gulani, and M. A. Griswold, "Simultaneous T1, T2, diffusion and proton density quantification with MR fingerprinting," in *Proc. ISMRM*, Milan, Italy, 2014.
- [16] P. Su, D. Mao, P. Liu, Y. Li, M. C. Pinho, B. G. Welch, and H. Lu, "Multiparametric estimation of brain hemodynamics with MR fingerprinting ASL," *Magn. Reson. Med.*, vol. 78, no. 5, pp. 1812–1823, 2017.
- [17] J. I. Hamilton and N. Seiberlich, "MR fingerprinting with chemical exchange (MRF-X) for in vivo multi-compartment relaxation and exchange rate mapping," in *Proc. ISMRM*, Singapore, 2016.
- [18] G. Buonincontri and S. J. Sawiak, "MR fingerprinting with simultaneous B1 estimation," *Magn. Reson. Med.*, vol. 76, no. 4, pp. 1127–1135, Oct. 2016.
- [19] D. Ma, S. Coppo, Y. Chen, D. F. McGivney, Y. Jiang, S. Pahwa, V. Gulani, and M. A. Griswold, "Slice profile and B1 corrections in 2D magnetic resonance fingerprinting," *Magn. Reson. Med.*, vol. 78, no. 5, pp. 1781–1789, 2017.
- [20] S. F. Cauley, K. Setsompop, D. Ma, Y. Jiang, H. Ye, E. Adalsteinsson, M. A. Griswold, and L. L. Wald, "Fast group matching for MR fingerprinting reconstruction," *Magn. Reson. Med.*, vol. 74, no. 2, pp. 523–528, 2015.
- [21] D. F. McGivney, E. Pierre, D. Ma, Y. Jiang, H. Saybasili, V. Gulani, and M. A. Griswold, "SVD Compression for Magnetic Resonance Fingerprinting in the Time Domain," *IEEE Trans. Med. Imaging*, vol. 33, no. 12, pp. 2311–2322, Dec. 2014.
- [22] M. Yang, D. Ma, Y. Jiang, J. Hamilton, N. Seiberlich, M. A. Griswold, and D. McGivney, "Low rank approximation methods for MR fingerprinting with large scale dictionaries," *Magn. Reson. Med.*, Aug. 2017.
- [23] M. Unser, "Splines: A perfect fit for signal and image processing," *IEEE Signal Process. Mag.*, vol. 16, no. 6, pp. 22–38, 1999.
- [24] W. Huizinga, S. Klein, and D. H. J. Poot, "Fast Multidimensional B-spline Interpolation Using Template Metaprogramming," in *WBIR*, 2014, pp. 11–20.
- [25] K. E. Keenan, K. F. Stupic, M. A. Boss, S. E. Russek, T. L. Chenevert, P. V. Prasad, W. E. Reddick, J. Zheng, P. Hu, and E. F. Jackson, "Comparison of T1 measurement using ISMRM/NIST system phantom," in *Proc. ISMRM*, Singapore, 2016.

- [26] J. I. Hamilton, Y. Jiang, Y. Chen, D. Ma, W.-C. Lo, M. Griswold, and N. Seiberlich, “MR fingerprinting for rapid quantification of myocardial T1, T2, and proton spin density,” *Magn. Reson. Med.*, vol. 77, no. 4, pp. 1446–1458, Apr. 2017.
- [27] P. Tofts, *Quantitative MRI of the brain: measuring changes caused by disease*. John Wiley & Sons, 2005.
- [28] A. Van den Bos, *Parameter estimation for scientists and engineers*. John Wiley & Sons, 2007.
- [29] W. A. Edelstein, P. A. Bottomley, H. R. Hart, and L. S. Smith, “Signal, noise, and contrast in nuclear magnetic resonance (NMR) imaging,” *J Comput Assist Tomogr*, vol. 7, no. 3, pp. 391–401, Jun. 1983.
- [30] M. O’Donnell, J. C. Gore, and W. J. Adams, “Toward an automated analysis system for nuclear magnetic resonance imaging. I. Efficient pulse sequences for simultaneous T1–T2 imaging,” *Medical Physics*, vol. 13, no. 2, pp. 182–190, Mar. 1986.
- [31] A. P. Crawley and R. M. Henkelman, “A comparison of one-shot and recovery methods in T1 imaging,” *Magn. Reson. Med.*, vol. 7, no. 1, pp. 23–34, May 1988.
- [32] Nielsen Jon-Fredrik and Noll Douglas C., “TOPPE: A framework for rapid prototyping of MR pulse sequences,” *Magnetic Resonance in Medicine*, vol. 79, no. 6, pp. 3128–3134, Mar. 2018.
- [33] J. A. Jones, P. Hodgkinson, A. L. Barker, and P. J. Hore, “Optimal Sampling Strategies for the Measurement of Spin–Spin Relaxation Times,” *Journal of Magnetic Resonance, Series B*, vol. 113, no. 1, pp. 25–34, Oct. 1996.
- [34] A. Anastasiou and L. D. Hall, “Optimisation of T2 and M0 measurements of bi-exponential systems,” *Magnetic Resonance Imaging*, vol. 22, no. 1, pp. 67–80, Jan. 2004.
- [35] A. N. Dula, D. F. Gochberg, and M. D. Does, “Optimal echo spacing for multi-echo imaging measurements of Bi-exponential T2 relaxation,” *Journal of Magnetic Resonance*, vol. 196, no. 2, pp. 149–156, Feb. 2009.
- [36] F. Baselice, G. Ferraioli, A. Grassia, and V. Pascasio, “Optimal Configuration for Relaxation Times Estimation in Complex Spin Echo Imaging,” *Sensors*, vol. 14, no. 2, pp. 2182–2198, Jan. 2014.
- [37] M. Akçakaya, S. Weingärtner, S. Roujol, and R. Nezafat, “On the selection of sampling points for myocardial T1 mapping,” *Magnetic Resonance in Medicine*, vol. 73, no. 5, pp. 1741–1753, May 2015.
- [38] G. Nataraj, J.-F. Nielsen, and J. Fessler, “Optimizing MR Scan Design for Model-Based T1, T2 Estimation from Steady-State Sequences,” *IEEE Transactions on Medical Imaging*, pp. 1–1, 2016.
- [39] Y. Liu, J. R. Buck, and V. N. Ikonomidou, “Generalized min-max bound-based MRI pulse sequence design framework for wide-range T1 relaxometry: A case study on the tissue specific imaging sequence,” *PLOS ONE*, vol. 12, no. 2, p. e0172573, Feb. 2017.

- [40] R. P. A. G. Teixeira, S. J. Malik, and J. V. Hajnal, “Joint system relaxometry (JSR) and Crámer-Rao lower bound optimization of sequence parameters: A framework for enhanced precision of DES-POT T1 and T2 estimation,” *Magnetic Resonance in Medicine*, vol. 79, no. 1, pp. 234–245, Jan. 2018.
- [41] B. Zhao, J. P. Haldar, C. Liao, D. Ma, Y. Jiang, M. A. Griswold, K. Setsompop, and L. L. Wald, “Optimal Experiment Design for Magnetic Resonance Fingerprinting: Cramér-Rao Bound Meets Spin Dynamics,” *IEEE Transactions on Medical Imaging*, pp. 1–1, 2018.
- [42] O. Brihuega-Moreno, F. P. Heese, and L. D. Hall, “Optimization of diffusion measurements using Cramér-Rao lower bound theory and its application to articular cartilage,” *Magnetic Resonance in Medicine*, vol. 50, no. 5, pp. 1069–1076, Nov. 2003.
- [43] D. C. Alexander, “A general framework for experiment design in diffusion MRI and its application in measuring direct tissue-microstructure features,” *Magn. Reson. Med.*, vol. 60, no. 2, pp. 439–448, Aug. 2008.
- [44] D. H. J. Poot, A. J. den Dekker, E. Achten, M. Verhoye, and J. Sijbers, “Optimal Experimental Design for Diffusion Kurtosis Imaging,” *IEEE Transactions on Medical Imaging*, vol. 29, no. 3, pp. 819–829, Mar. 2010.
- [45] D. De Naeyer, Y. De Deene, W. P. Ceelen, P. Segers, and P. Verdonck, “Precision analysis of kinetic modelling estimates in dynamic contrast enhanced MRI,” *Magn Reson Mater Phy*, vol. 24, no. 2, pp. 51–66, Apr. 2011.
- [46] M. Cercignani and D. C. Alexander, “Optimal acquisition schemes for in vivo quantitative magnetization transfer MRI,” *Magnetic Resonance in Medicine*, vol. 56, no. 4, pp. 803–810, Oct. 2006.
- [47] K. Li, Z. Zu, J. Xu, V. A. Janve, J. C. Gore, M. D. Does, and D. F. Gochberg, “Optimized inversion recovery sequences for quantitative T1 and magnetization transfer imaging,” *Magn. Reson. Med.*, vol. 64, no. 2, pp. 491–500, Aug. 2010.
- [48] A. R. Pineda, S. B. Reeder, Z. Wen, and N. J. Pelc, “Cramér–Rao bounds for three-point decomposition of water and fat,” *Magn. Reson. Med.*, vol. 54, no. 3, pp. 625–635, Sep. 2005.
- [49] C. Wyatt, B. J. Soher, K. Arunachalam, and J. MacFall, “Comprehensive analysis of the Cramer–Rao bounds for magnetic resonance temperature change measurement in fat–water voxels using multi-echo imaging,” *Magn Reson Mater Phy*, vol. 25, no. 1, pp. 49–61, Feb. 2012.
- [50] I. Kay and R. M. Henkelman, “Practical Implementation and Optimization of One-shot T1 imaging,” *Magn. Reson. Med.*, vol. 22, no. 2, pp. 414–424, Dec. 1991.
- [51] N. Stikov, M. Boudreau, I. R. Levesque, C. L. Tardif, J. K. Barral, and G. B. Pike, “On the accuracy of T1 mapping: Searching for common ground,” *Magn. Reson. Med.*, vol. 73, no. 2, pp. 514–522, Feb. 2015.
- [52] H. Wang and Y. Cao, “Spatially regularized T1 estimation from variable flip angles MRI,” *Med Phys*, vol. 39, no. 7, pp. 4139–4148, Jul. 2012.

- [53] L. I. Sacolick, F. Wiesinger, I. Hancu, and M. W. Vogel, "B1 mapping by Bloch-Siegert shift," *Magn. Reson. Med.*, vol. 63, no. 5, pp. 1315–1322, May 2010.
- [54] A. M. Peters, M. J. Brookes, F. G. Hoogenraad, P. A. Gowland, S. T. Francis, P. G. Morris, and R. Bowtell, "T2\* measurements in human brain at 1.5, 3 and 7 T," *Magnetic Resonance Imaging*, vol. 25, no. 6, pp. 748–753, Jul. 2007.
- [55] M. S. Sussman, L. Vidarsson, J. M. Pauly, and H.-L. M. Cheng, "A technique for rapid single-echo spin-echo T2 mapping," *Magnetic Resonance in Medicine*, vol. 64, no. 2, pp. 536–545, 2010.
- [56] W. van Valenberg, S. Klein, F. M. Vos, K. Koolstra, L. J. van Vliet, and D. H. J. Poot, "An Efficient Method for Multi-Parameter Mapping in Quantitative MRI using B-Spline Interpolation," *IEEE Transactions on Medical Imaging*, 2019.
- [57] G. J. Stanisz, E. E. Odrobina, J. Pun, M. Escaravage, S. J. Graham, M. J. Bronskill, and R. M. Henkelman, "T1, T2 relaxation and magnetization transfer in tissue at 3T," *Magn. Reson. Med.*, vol. 54, no. 3, pp. 507–512, Sep. 2005.



## Summary

Magnetic resonance imaging (MRI) is the primary modality for the imaging of soft tissues (e.g. brain, muscle, liver). Therefore, it is an essential radiological tool for diagnosis and surgical planning. The contrast in MR images is due to tissues responding differently to the magnetic fields generated by the scanning system. This response can be described by the physical properties of the tissue (e.g. proton density, magnetic relaxation) and the magnetic fields. These physical properties are represented by multiple parameters that can be estimated through quantitative MRI (qMRI) methods. The parameters are considered more reproducible than conventional MR images, which simplifies the comparison of MR data from different subjects or scanning systems. Estimating multiple parameters simultaneously is needed to reduce error from system imperfections and deliver accurate estimates of the physical tissue parameters.

Although qMRI methods have been available for many years, there are still few clinical applications. This is due to the long scan time required for measuring multiple parameters with conventional qMRI methods. Furthermore, the simultaneous estimation of multiple parameters is computationally challenging due to time and memory constraints.

## Samenvatting

Magnetische resonantie (MRI) is de belangrijkste methode voor de beeldvorming van zachte weefsels zoals hersenen, spieren, en lever. Daarom is het een essentieel radiologisch middel voor medische diagnose en de planning van operaties. Contrast in MR-beelden ontstaat doordat weefsels verschillend reageren op de magnetische velden die door het MR-systeem worden gegenereerd. Deze reactie wordt bepaald door de fysische eigenschappen van zowel het weefsel (zoals de dichtheid van de protonen en de magnetische relaxatie) als de magnetische velden. De fysische eigenschappen zijn uit te drukken in verschillende parameters die we kunnen schatten met kwantitatieve MRI (qMRI) methoden. Deze parameters worden als beter reproduceerbaar beschouwd dan normale MR-beelden, wat het vergelijken van scans tussen verschillende mensen of MR-systemen vereenvoudigt. Het gelijktijdig schatten van meerdere parameters is nodig om versturende effecten van systeem-imperfecties te verminderen en om accurate schattingen van de fysieke weefselparameters te leveren.

Ondanks dat qMRI-methoden al vele jaren beschikbaar zijn, zijn er nog weinig klinische toepassingen. Dit komt door de lange scantijd vereist voor het meten van meerdere parameters met conventionele qMRI-methoden. Bovendien is de gelijktijdige schatting van meerdere parameters een uitdaging voor de computer vanwege tijd-

This thesis presents a number of new techniques for the reproducible estimation of multiple physical MRI parameters, which increases the applicability of qMRI methods to the clinic.

In Chapter 2, we simplified the simultaneous estimation of multiple parameters using an efficient interpolation method. This new method allows reducing the computational and memory costs of estimating the MRI parameters and thus improves the feasibility of accurate multi-parametric mapping. This chapter provided the basis for the methods of the Chapters 3 and 4.

There is a large selection of qMRI methods that differ in accuracy (i.e. bias), precision (estimation variance), acquisition time, and features like motion sensitivity, gating capabilities and/or fat suppression. This makes determining the best method for parameter estimation difficult. In Chapter 3, we proposed a selection criterion, called time efficiency, that reflects the precision that can be achieved in the available scan time. The predicted time efficiencies are shown to be representative for a range of qMRI methods and estimated parameters. Hence, with this proposed measure, selection of the best method as well as its settings can be performed *in-silico*, which avoids costly evaluations on the scanner.

Conventionally, the quantification of the physical processes that determine the

en geheugenbeperkingen. Dit proefschrift presenteert een aantal nieuwe technieken voor het reproduceerbare schatten van meerdere fysieke MRI-parameters. Dit moet de toepasbaarheid van qMRI-methoden voor de kliniek verhogen.

In hoofdstuk 2 vereenvoudigen we de gelijktijdige schatting van meerdere parameters met behulp van een efficiënte interpolatiemethode. Deze nieuwe methode maakt het mogelijk de reken- en geheugenkosten van het schatten van de parameters te verlagen en maakt de nauwkeurige schatting van meerdere parameters mogelijk. Dit hoofdstuk vormde de basis voor de methoden van de hoofdstukken 3 en 4.

Er is een grote selectie van qMRI-methoden die verschillen in nauwkeurigheid, precisie, scantijd, en eigenschappen zoals de gevoeligheid voor beweging en de mogelijkheid om vet te onderdrukken. Dit maakt het bepalen van de beste methode voor het schatten van parameters lastig. In hoofdstuk 3 hebben we een selectiecriteria voorgesteld, genaamd tijdsefficiëntie, dat de precisie beschrijft die kan worden bereikt in de beschikbare scantijd. De voorspelde en gemeten tijdsefficiënties komen overeen voor vele soorten qMRI-methoden en geschatte parameters. Daarom kan door middel van deze maat de selectie van de beste methode en instellingen worden bepaald op de computer, waardoor kostbare evaluaties op de scanner worden vermeden.

Gewoonlijk wordt de kwantificering van de fysieke processen die het MR-sigitaal bepa-

MR signal are done through a dedicated qMRI method for each parameter. When multiple qMRI parameters are of interest, each parameter may be estimated separately or in some cases sequentially. In Chapter 4 we study the simultaneous estimation of multiple parameters by combining several quantitative methods. We propose a framework to select the optimal combination of quantitative MRI methods as well as their settings to obtain maximal precision for a certain set of quantitative parameters. We found that an optimal combination of quantitative methods had higher (expected) precisions for the estimated parameters than most dedicated methods have for a single parameter, while requiring similar scan time.

This thesis shows that quantitative methods are rapidly maturing: obtaining more accurate and precise estimates in shorter scan times. Application of the proposed methods in clinical and population studies are now required in order to make the next step towards regular clinical use.

len, uitgevoerd via specifieke qMRI-methodes voor elke parameter. Wanneer meerdere qMRI-parameters van belang zijn, kan elke parameter afzonderlijk of in sommige gevallen achtereenvolgens worden geschat. In hoofdstuk 4 bekijken we de gelijktijdige schatting van meerdere parameters door middel van het combineren van verschillende kwantitatieve methoden. We presenteren een manier om de optimale combinatie van kwantitatieve MRI-methoden en hun instellingen te selecteren die de maximale nauwkeurigheid heeft voor een bepaalde set kwantitatieve parameters. We vonden dat een optimale combinatie van kwantitatieve methoden een hogere (verwachte) precisie had voor de geschatte parameters dan de meeste specifieke methoden voor een enkele parameter hebben, terwijl ze dezelfde scantijd hebben.

Dit proefschrift laat zien dat kwantitatieve methoden snel ontwikkelen: ze verkrijgen steeds nauwkeurigere en preciezere schattingen in minder scantijd. Toepassing van de gepresenteerde methoden in klinische en populatiestudies is nu vereist om de volgende stap te zetten naar breed klinisch gebruik.

